Impact of DEM-Assisted Coregistration on High-Resolution SAR Interferometry

Davide Oscar Nitti, Ramon F. Hanssen, *Member, IEEE*, Alberto Refice, Fabio Bovenga, and Raffaele Nutricato

Abstract—Image alignment is a crucial step in synthetic aperture radar (SAR) interferometry. Interferogram formation requires images to be coregistered with an accuracy of better than a few tenths of a resolution cell to avoid significant loss of phase coherence. In conventional interferometric precise coregistration methods for full-resolution SAR data, a 2-D polynomial of low degree is usually chosen as warp function, and the polynomial parameters are estimated through least squares fit from the shifts measured on image windows. In case of rough topography or long baselines, the polynomial approximation may become inaccurate, leading to local misregistrations. These effects increase with spatial resolution of the sensor. An improved elevation-assisted image-coregistration procedure can be adopted to provide better prediction of the offset vectors. This approach computes pixel by pixel the correspondence between master and slave acquisitions by using the orbital data and a reference digital elevation model (DEM). This paper aims to assess the performance of this procedure w.r.t. the "standard" one based on polynomial approximation. Analytical relationships and simulations are used to evaluate the improvement of the DEM-assisted procedure w.r.t. the polynomial approximation as well as the impact of the finite vertical accuracy of the DEM on the final coregistration precision for different resolutions and baselines. The two approaches are then evaluated experimentally by processing high-resolution SAR data provided by the COnstellation of small Satellites for the Mediterranean basin Observation (COSMO/SkyMed) and TerraSAR-X missions, acquired over mountainous areas in Italy and Tanzania, respectively. Residual-range pixel offsets and interferometric coherence are used as quality figure.

Index Terms—Coregistration, digital elevation model (DEM), interferometry, synthetic aperture radar (SAR).

I. INTRODUCTION

SYNTHETIC aperture radar (SAR) interferometry (InSAR) is the study of coherent combinations of SAR images taken from slightly different observation directions. Precise (subpixel) image alignment is then required as a first processing step [1]. High-accuracy image coregistration is a requirement common to many other fields of remote sensing [2] and even to other applications of signal processing, such as medical imaging [3], where multiimage data sets are used to detect subtle temporal or geometric changes in objects or scenes. For a general review of image-registration techniques, see [4] and the references therein. Precise coregistration of SAR images is a nontrivial task since a change in radar-acquisition geometry generates image shifts, which, in principle, depend on the topography [5]. Many methods have been developed to deal with the problem. One of the most used approaches relies on the fact that SAR images suitable for interferometry are separated by relatively small geometric baselines (compared, e.g., with radargrammetric processing [5]). In this case, when topographic variations are not too strong, the change in acquisition geometry from one image to the other can be approximated by a low-order polynomial transformation. The polynomial coefficients are usually estimated by least squares fitting of a series of image pixel-offset values, measured on several image patches distributed across the scene. Such offsets are in turn estimated by locally maximizing a merit figure, such as the data cross correlation.

Minimizing coherence losses to improve coregistration performances is a long-term goal in InSAR research. In [6], a model for the coregistration quality as a function of spatial, temporal, and Doppler baselines is used as a score function to decide, through application of a minimum spanning tree structure, which images should be connected in small-baseline pairs; this allows minimizing baseline-decorrelation effects, optimizing image-to-image coregistration performances, and providing the processing sequence to finally obtain the coregistration parameters of image pairs separated by long baselines.

Alternative accurate coregistration methods available when dealing with critical interferometric conditions consist, e.g., in exploiting contrasted image features or ideal point scatterers [7], [8]. Other efficient methods exploit spectral-target diversity [9], [10]. The results are hardly applicable to satellite data characterized by small relative signal bandwidths [European Remote Sensing satellite (ERS), ENVIronmental SATellite (ENVISAT), and Advanced Land Observing Satellite (ALOS)], but are beginning to become feasible for applications to the new generation of X-band sensors [TerraSAR-X (TSX), COSMO/SkyMed (CSK)].

In this paper, we deal with a novel processing procedure which provides topography-based prediction of the pixel-offset vectors. Instead of estimating the shifts on a limited number of patches and then using a polynomial approximation for the transformation, this approach computes pixel by pixel the

D. O. Nitti is with the Dipartimento Interateneo di Fisica, Politecnico di Bari, 70126 Bari, Italy (e-mail: davide.nitti@fisica.uniba.it).

R. F. Hanssen is with the Department of Earth Observation and Space Systems, Delft University of Technology, 2629 Delft, The Netherlands.

A. Refice and F. Bovenga are with Consiglio Nazionale delle Ricerche-Istituto di Studi sui Sistemi Intelligenti per l'Automazione (CNR-ISSIA), 70126 Bari, Italy.

R. Nutricato is with Geophysical Applications Processing s.r.l., c/o Dipartimento Interateneo di Fisica, Politecnico di Bari, 70126 Bari, Italy.

correspondence between master and slave by using the orbital data and a reference digital elevation model (DEM). In fact, as shown in the following, the effectiveness of the polynomial approximation depends on the topography variation over the scene, on the length of the interferometric baseline, and on the spatial resolution of the imagery. Thus, for applications involving areas of rough topography and/or long baselines and particularly for the new high-resolution SAR satellites, the improvement given by correctly modeling topography-based image pixel offsets is considerable.

Various groups reported experiences with DEM-based In-SAR coregistration approaches [11]–[13], detecting some improvement w.r.t. more conventional methods, although to date, such assessments have been rather empirical. In this paper, we aim to assess the performance of the DEM-assisted coregistration approach w.r.t. the conventional procedure based on cross correlations and the approximated polynomial warp function. To do this, we develop a geometrical model allowing expressing analytically the shifts between a master and a slave SAR image for a given acquisition geometry and for any image pixel. This analytical model allows treating in a straightforward manner the error budgets associated with the two approaches, particularly the limited accuracy due to the polynomial approximation and the error due to the finite DEM precision. The theoretical performances of both approaches can thus be compared for several typical satellite configurations. The analytical considerations are then validated by showing results of coregistrations operated on X-band SAR acquisitions of both CSK and TSX missions since high-resolution data are most sensitive to misregistrations due to smooth warp functions.

The results are evaluated by comparing the residual pixel offsets as well as through the merit figure constituted by the interferometric coherence.

Real-data coregistration has been carried out by applying the DEM-assisted technique developed at the Delft University of Technology (TU Delft) [12] and recently implemented as part of the Delft Object-oriented Radar Interferometric Software (DORIS) [14].

This paper is organized as follows. In Section II, the geometrical model is described, and the analytical formulation of the relative shifts between two images are computed as a function of the mission parameters. Section III describes the expected performance results of the DEM-assisted approach by simulating different acquisition configurations. In particular, the theoretical coregistration error due to the polynomial approximation is evaluated as well as the effect of DEM errors on the final coregistration precision of the DEM-assisted approach. In Section IV, the conventional coregistration procedure and the DEM-assisted coregistration procedure are compared by processing CSK and TSX data. Comments and conclusions are provided in Section V.

II. ANALYTICAL FORMULATION

As mentioned in the preceding section, the relative disalignment between two SAR images acquired from two different orbits separated by a baseline B depends, in general, on the

local topographic elevation [5]. Operationally, this disalignment can be computed pixel by pixel through knowledge of the terrain elevation and precise orbital-satellite positions. Orbit and elevation data are usually given in a reference frame in which the Earth is modeled as an ellipsoid (e.g., WGS84). In [12] and other works [15], the performances of the DEM-assisted method w.r.t. conventional correlation-based coregistration is illustrated through application to test sites characterized by different locations and topography. Here, we introduce a geometric model to calculate the range shifts between master and slave images as a function of the 3-D position of any given point on the Earth surface. Using an ellipsoidal model for the Earth to compute the image shifts gives rise to equations which cannot be easily treated analytically. Nevertheless, as shown in the following, spherical models can be used as a good local approximation of the ellipsoidal surface with negligible errors as long as the evaluation remains limited to the sensor swath extension. Using a spherical model greatly simplifies the equations for the image shifts to be estimated by the coregistration step. In this section, we introduce an approximated spherical model (Fig. 1), which is further refined in Appendix I-A, to derive the shift expressions in the assumption of zero-Doppler side-looking geometry.

All geometric parameters involved in the following discussion have to be computed in an *Earth-centered Earth-fixed* reference system $Oxyz$ (see Fig. 2), thus intrinsically taking into account the effect of the Earth's rotation. First of all, once the master slow-time instant is fixed, an initial choice for the radius ρ of the spherical model is the Earth curvature radius R_{az} of the nadir projection of the master-satellite position on the reference ellipsoid having geodetic coordinates Φ_M and Λ_M (Fig. 2).

The azimuth orientation angle of the intersection of the zero-Doppler plane (indicated as π-plane in the following) with the Earth ellipsoid is therefore equal to $\alpha_h + \pi/2$ (in case of right-looking sensor), where α_h is the inclination, or heading, of the orbit (measured clockwise from the north direction, see Fig. 2). The Earth curvature R_{az} corresponding to the section π is defined through Euler's theorem as [16]

$$\frac{1}{R_{az}} = \frac{\cos^2\left(\alpha_h + \frac{\pi}{2}\right)}{M} + \frac{\sin^2\left(\alpha_h + \frac{\pi}{2}\right)}{N} \qquad (1)$$

where M and N are the curvature radii of the meridian and the prime vertical, respectively, for the specific point $P_M^{nad}(\Phi_M, \Lambda_M)$ considered (Meusnier's theorem [17]), i.e.,

$$M = \frac{a(1-e^2)}{\sqrt[3]{1-e^2\sin^2\Phi_M}}$$

$$N = \frac{a}{\sqrt{1-e^2\sin^2\Phi_M}} \qquad (2)$$

and a, b, and e are the semiaxes and the first eccentricity of the reference ellipsoid, respectively.

In other words, for each master slow-time instant, the cross section between the corresponding zero-Doppler plane π and the reference ellipsoid is an ellipse that we are approximating,
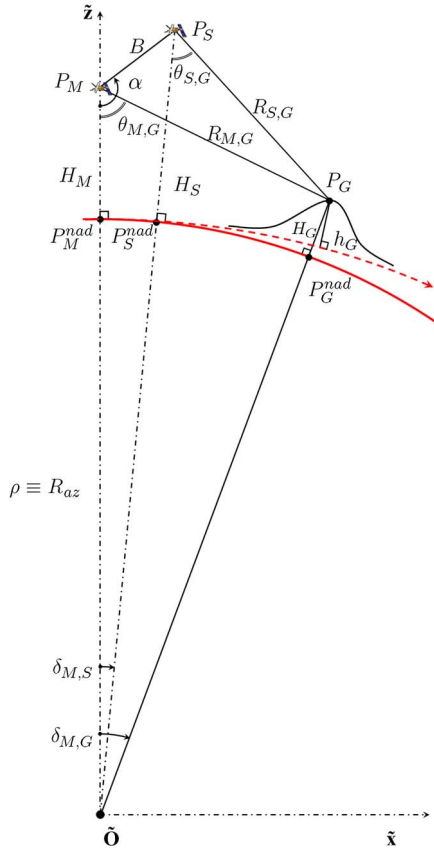
Fig. 1. SAR interferometric geometry. (Dashed red line) The intersection between the reference ellipsoid (WGS84) and the zero-Doppler plane π is approximated with (solid red line) a circle centered in $\tilde{O}$, the curvature center of the ellipse w.r.t. the nadir projection P_M^{nad} of the master satellite position. The ellipsoidic height of the ground target P_G, h_G, should not be confused with the corresponding height above the circular approximation H_G. The radius ρ of the spherical model is coincident with the Earth curvature radius R_{az} at the nadir projection P_M^{nad}. The position of the slave satellite is provided in terms of the baseline B and the baseline orientation angle α, measured from the master nadir direction toward the line of sight (LOS).

near the projection P_M^{nad}, by a circle of radius $\rho = R_{az}$, centered on the curvature center $\tilde{O}$ of the ellipse w.r.t. P_M^{nad}. For every point along the ground swath, the difference between the heights above the spherical approximation just defined H_G and the reference ellipsoid h_G is assumed to be negligible (Fig. 1). The limits of this assumption are discussed in Appendix I-A.

In the zero-Doppler plane π, we then define a new reference system $\tilde{O}\tilde{x}\tilde{z}$ (see Fig. 2), with the $\tilde{z}$-axis coincident with the zenithal direction of the master-satellite position and the $\tilde{x}$-axis normal to the first one, directed toward the looking direction of the radar. The coordinates of the origin $\tilde{O}$ of this new reference frame in the $Oxyz$ reference system are

$$
\begin{bmatrix} x_{\tilde{O}} \\ y_{\tilde{O}} \\ z_{\tilde{O}} \end{bmatrix} = \begin{bmatrix} r_{x\tilde{x}} & r_{x\tilde{y}} & r_{x\tilde{z}} \\ r_{y\tilde{x}} & r_{y\tilde{y}} & r_{y\tilde{z}} \\ r_{z\tilde{x}} & r_{z\tilde{y}} & r_{z\tilde{z}} \end{bmatrix} \times \begin{bmatrix} 0 \\ 0 \\ N - R_{az} \end{bmatrix} + \begin{bmatrix} 0 \\ 0 \\ \frac{-\tan\Phi_M(a^2 - b^2)}{\sqrt{a^2 + b^2 \tan^2\Phi_M}} \end{bmatrix} \quad (3)
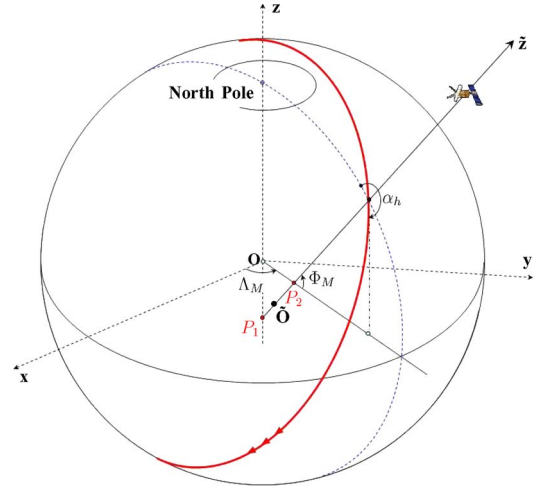$$

Fig. 2. Three-dimensional view of the SAR acquisition mode (stripmap mode). For a given azimuth time, the scene imaged by the radar along the LOS belongs to the zero-Doppler plane π. Because of the side-looking acquisition mode of SAR sensors and the assumption of zero-Doppler (deskewed) stripmap-imaging geometry, the azimuth angle of the cross section π is equal to $(\alpha_h + \pi/2)$ (in case of right looking), with α_h heading of the orbit. $\tilde{O}$ is the curvature center in the nadir projection of the master-satellite position P_M^{nad}. In practice, $\tilde{O}$ is always located along the nadir direction, between points P_1 (center of curvature of the prime vertical in P_M^{nad}) and P_2, depending on the particular azimuth angle of the section π.

where the matrix of coefficients $r_{i\tilde{j}}$ is given by

$$
\begin{bmatrix} r_{x\tilde{x}} & r_{x\tilde{y}} & r_{x\tilde{z}} \\ r_{y\tilde{x}} & r_{y\tilde{y}} & r_{y\tilde{z}} \\ r_{z\tilde{x}} & r_{z\tilde{y}} & r_{z\tilde{z}} \end{bmatrix} = \begin{bmatrix} \sin\Lambda_M & \cos\Lambda_M & 0 \\ -\cos\Lambda_M & \sin\Lambda_M & 0 \\ 0 & 0 & 1 \end{bmatrix}
$$
$$
\times \begin{bmatrix} 1 & 0 & 0 \\ 0 & \sin\Phi_M & \cos\Phi_M \\ 0 & -\cos\Phi_M & \sin\Phi_M \end{bmatrix} \times \begin{bmatrix} -\cos\alpha_h & -\sin\alpha_h & 0 \\ \sin\alpha_h & -\cos\alpha_h & 0 \\ 0 & 0 & 1 \end{bmatrix}. \quad (4)
$$

Using this geometric model, assuming that precise orbits and a DEM, which is radar coded in the master geometry, are available, it is possible to retrieve analytically the pixel offset between master and slave along the slant-range direction at each specific master slow-time instant, as described further on. For avoiding nonessential complications in the following equations, the orbits are assumed to be parallel, and the SAR images are registered in zero-Doppler geometry when focused.

Our aim is to estimate, for each master pixel number p_M, the corresponding slave pixel-position number p_S and, so, the relative offset in the range $\Delta p = p_S - p_M$. We are interested in evaluating the influence of the baseline (particularly its normal component) on the range pixel offsets. Therefore, a description of the slave-satellite position in terms of relative position w.r.t. the master satellite is preferable. With B, we indicate the distance (baseline) between master and slave, while α is the off-nadir baseline orientation angle measured toward the SAR looking direction. The slave height H_S is related to the master height H_M, baseline, and baseline orientation angle by the following relation:

$$
\rho + H_S = \sqrt{(\rho + H_M)^2 + B^2 - 2B(\rho + H_M)\cos\alpha}. \quad (5)
$$

For a given pixel number p_σ (where $p_\sigma = 0, \ldots, N_{p_\sigma} - 1$ and $\sigma \in \{M, S\}$, with M = Master and S = Slave), the master and slave slant-range distances $R_{\sigma,G}$ are related to the corresponding two-way zero-Doppler range times τ_{p_σ} (or fast times) through

$$\tau_{p_\sigma} = \tau_{\sigma 0} + \frac{p_\sigma}{f_s}$$
$$R_{\sigma,G} = \frac{c}{2}\tau_{p_\sigma} = \frac{c}{2}\left(\tau_{\sigma 0} + \frac{p_\sigma}{f_s}\right) \tag{6}$$

where c is the speed of light, f_s is the range sampling rate, and $\tau_{\sigma 0}(\sigma \in \{M, S\})$ are the two-way zero-Doppler range times for the first range pixels. Pixel offsets between the master and slave along the range direction are hence given by

$$\begin{aligned}
\Delta p &= p_S - p_M \\
&= f_s \left(2\frac{R_{S,G}}{c} - \tau_{S0}\right) - p_M \\
&= f_s \left[\frac{2}{c}(R_{S,G} - R_{M,G}) + (\tau_{M0} - \tau_{S0})\right]. \tag{7}
\end{aligned}$$

For each master pixel p_M, the main problem is finally the estimation of the distance $R_{S,G}$ between the slave satellite and the ground point G, whose height above the spherical model and distance from the master satellite are equal to H_G and $R_{M,G}$, respectively. This can be accomplished by observing that (Fig. 1)

$$\begin{aligned}
\frac{\sin \delta_{M,S}}{B} &= \frac{\sin \alpha}{\rho + H_S} \\
\frac{\sin \delta_{M,G}}{R_{M,G}} &= \frac{\sin \theta_{M,G}}{\rho + H_G} \\
\frac{\sin(\delta_{M,G} - \delta_{M,S})}{R_{S,G}} &= \frac{\sin \theta_{S,G}}{\rho + H_G} \\
\cos^2 \theta_{\sigma,G} &= \frac{(\rho + H_\sigma)^2 + R_{\sigma,G}^2 - (\rho + H_G)^2}{2R_{\sigma,G}(\rho + H_\sigma)} \tag{8}
\end{aligned}$$

where $\delta_{\sigma,G}$ and $\theta_{\sigma,G}$ are the look angles of the ground point G from, respectively, the curvature center $\tilde{O}$ and the satellites positions (Fig. 1). For each master pixel p_M, $R_{M,G}$ is expressed by (6), and $R_{S,G}$ can be estimated numerically by combining (8) into

$$\begin{aligned}
&\arcsin\left[\frac{R_{M,G}}{\rho + H_G}\sqrt{1 - \frac{(\rho + H_M)^2 + R_{M,G}^2 - (\rho + H_G)^2}{2R_{M,G}(\rho + H_M)}}\right] \\
&-\arcsin\left[\frac{R_{S,G}}{\rho + H_G}\sqrt{1 - \frac{(\rho + H_S)^2 + R_{S,G}^2 - (\rho + H_G)^2}{2R_{S,G}(\rho + H_S)}}\right] \\
&= \arcsin\frac{B\sin\alpha}{\rho + H_S} \tag{9}
\end{aligned}$$

and solving for $R_{S,G}$.

In summary, the pixel offset between master and slave can be expressed, through (7)–(9), as the product of the range sampling

rate and a function of the normal and parallel baselines as well as the topographic height H_G above the spherical model adopted (by assumption, very close to the height h_G above the reference ellipsoid).

As a final comment, it can be proved that the aforementioned model reduces to the well-known expressions in the limiting cases of prevailingly parallel or perpendicular baselines. To show this, we write the expressions of the parallel and perpendicular components of the baseline as a function of the look angle $\theta_{M,G}$

$$\begin{aligned}
B_\perp &= B\sin(\alpha - \theta_{M,G}) \\
B_\parallel &= B\cos(\alpha - \theta_{M,G}) \\
B\sin\alpha &= B_\perp \cos\theta_{M,G} + B_\parallel \sin\theta_{M,G} \\
B\cos\alpha &= B_\parallel \cos\theta_{M,G} - B_\perp \sin\theta_{M,G}. \tag{10}
\end{aligned}$$

Then, in the limiting cases $|B_\parallel| \ll |B_\perp| \approx B$ or $|B_\perp| \ll |B_\parallel| \approx B$, (9) can be simplified as follows:

$$R_{S,G} \approx \begin{cases} R_{M,G} - B_\parallel, & \text{if } |B_\parallel| \gg |B_\perp| \\ \sqrt{R_{M,G}^2 + B_\perp^2}, & \text{if } |B_\parallel| \ll |B_\perp|. \end{cases} \tag{11}$$

III. PERFORMANCE EVALUATION

Having set up the geometrical model through (7)–(9), possibly refined through the substitutions in (A3) and (A4), we can apply analytical error-propagation methods to infer the effects of parameter accuracy. Having postulated perfect knowledge of orbit geometry, the only difference between the traditional polynomial-based and the DEM-assisted coregistration procedures are related to the warp-function smoothness and the DEM height accuracy, respectively. In this section, we analyze these two contributions.

A. Effects of the Warp-Function Smoothness

The analytical formulation described in the previous section allows estimating the actual offset in pixels along the slant range $\Delta p = p_S - p_M$ between the master and slave images at any slow-time instant. Therefore, the effectiveness of any kind of warp function in terms of its capability to fit the true geometric distortions can be analyzed w.r.t. any terrain profile. Then, we can investigate the effect of the warp functions $\Delta \tilde{p}_{\text{pol}}$ described by polynomials of a certain degree n, whose coefficients A_k are estimated in order to best fit (least squares approach) the actual offsets Δp, estimated on the data, from near to far range

$$\Delta p \approx \Delta \tilde{p}_{\text{pol}} = \sum_{k=0}^{n} A_k p_M^k. \tag{12}$$

In particular, we are interested in evaluating the impact of coregistration errors ($\epsilon_{\text{pol}}^p = \Delta \tilde{p}_{\text{pol}} - \Delta p$) on the interferometric phase whose coherence is related to misregistration in terms of resolution cells (δr). Our formulation, according to the usual processing outputs, refers to pixels which are related to the sampling frequency f_s. Although, in general, f_s can be

arbitrary provided that the Nyquist criterion is met, for SAR data, this parameter is strongly related to the range bandwidth $B_r : f_s = k \cdot B_r$, with k being close to 1 (e.g., $k = 1.22$ for the ERS/ENVISAT, $k = 1.14$ for ALOS Phased Array type L-band SAR (PALSAR), and $k = 1.10$ for TSX). In the following, we assume to deal with SAR images sampled by the nominal frequency rate. Thus, the results on misregistration evaluated in pixels can be easily interpreted in terms of resolution cells: ($\epsilon_{\text{pol}}^p = k \cdot \epsilon_{\text{pol}}^{\delta r}$).

The fit is also poor for very regular terrain profiles in case of high normal baselines and strong differences between the maximum and the minimum topographic height over the scene ΔH_G. This can be shown by modeling, for example, the terrain profile over the entire swath as a raised cosine, centered at midrange and with spatial period equal to the swath width. The results are summarized and shown in Fig. 3(a) and (b) for SAR sensors with different carrier frequencies, spatial resolutions, range sampling rates, and swath widths, hypothesizing a topographic range ΔH_G of 1 km over the entire swath and polynomial degrees $n \in \{2, 3\}$. In particular, simulation tests have been carried out for C-band sensors, such as the ERS and ENVISAT missions of the European Space Agency (ESA), for L-band, such as the ALOS mission of the Japanese Aerospace Exploration Agency (JAXA), and for the two X-band missions TSX and CSK. A first simulation consists in fixing the baseline B (1 km in Fig. 3) and varying the baseline orientation angle α from 0° to 360°. Hence, maximum misregistrations may be derived for the entire range of normal baselines $|B_\perp|$ from zero to B. Therefore, for any baseline orientation angle, the normal baseline and pixel-offset residual values can be derived from the polar diagrams in Fig. 3(a) and (b). The plots show that pixel-offset residuals increase with the normal baseline $|B_\perp|$, the height range ΔH_G over the scene, and the chirp bandwidth.

Because of the multibeam capability of all SAR sensors, except for ERS-1/2 missions, a choice has been done for the off-nadir angle. For ENVISAT data, Image-mode Swath 2 (IS2) is selected since it is the default stripmap acquisition mode for this sensor and compatible with the ERS side-looking geometry. According to the actual JAXA acquisition policy, strip #07 has been selected since it is the fine-beam single polarization default mode (off-nadir angle: 34.3°). Finally, for X-band missions, there is no default beam in the stripmap mode. In this case, the side-looking geometry of the processed TSX data has been chosen (see Section IV-A). The diagrams shown in Fig. 3(a) and (b) confirm that a DEM-assisted approach is highly preferable for a proper coregistration of X-band SAR images, even in the case of moderate values for $|B_\perp|$ and ΔH_G, since the offset residuals cannot be reduced under 1/8 resolution cell without resorting to polynomials of a degree that is much higher than three, which increases significantly the computational load. Moreover, even if a higher degree can most likely reduce the residuals, it leads, in general, to unstable solutions because of the excessive number of coefficients to be estimated. Misregistrations of more than 1/8 resolution cell never occurred, instead, for ERS images, with a third-degree polynomial and a topographic range of 1 km, even with normal baselines near to the critical value. Nevertheless, even for ERS images, the minimum required accuracy for a proper coreg-

istration could be hardly achievable with higher topographic ranges and/or a second-degree polynomial. Anyway, substantial improvements in the coregistration of ERS images are not easy to detect through the interferometric coherence since they are counterbalanced by the geometrical decorrelation because of the small value, in absolute terms, of the critical baseline (∼1.1 km for flat terrain). The polar diagrams in Fig. 3(a) and (b) reveal that, despite the doubled chirp bandwidth, the entity of misregistrations for a given parameter triplet $\{|B_\perp|, \Delta H_G, n\}$ for PALSAR is comparable with the corresponding residuals for the ERS satellite. This is explained in terms of the different side-looking geometry considered: PALSAR simulations refer, indeed, to an incidence angle of ∼ 38.7°, while the same angle is only ∼23.2° for ERS data. However, the polar diagrams refer to normal baselines that is not longer than 1 km, while PALSAR acquisition pairs with normal baselines of up to a few kilometers are not unusual [18]. Even the coregistration of ALOS interferograms should significantly improve when a DEM-assisted approach is adopted. Owing to the longer wavelength w.r.t. the C- and X-bands, the ALOS critical baseline is ∼15 km. This, in turn, leads to effective improvements in the measured interferometric coherence since the geometrical decorrelation could be considered quite negligible even with long baselines. The simulation tests so far described may be further extended and repeated by varying also the height range over the imaged scene. In Fig. 4, the maximum misregistrations thus estimated for both the alignment approaches are shown for a wide range of normal baselines (0 ÷ 1 km) and topographic levels (0 ÷ 3 km). The results confirm that even for ERS/ENVISAT interferometry, DEM-assisted coregistration may provide better accuracy when the swath covers mountainous areas with topographic ranges higher than 1 ÷ 2 km. The mentioned diagrams may be useful as a quick-and-dirty estimator when deciding whether the DEM-assisted approach (whose computational cost is much higher than the conventional one) is necessary for a proper image alignment.

B. DEM Error Analysis

The height information in the radar-coded DEM is affected by errors mainly due to the intrinsic finite vertical accuracy of the DEM and, to a lesser degree, to the accuracy of the radar-coding procedure. For instance, the Shuttle Radar Topography Mission (SRTM) provided Digital Terrain Elevation Data-2 DEMs, with a posting of 90×90 m (outside the U.S.) and 15-m absolute-height accuracy for most of the Earth's surface; as we will see, such accuracy is sufficient for our registration purposes. In this section, we estimate the entity of pixel-offset residuals for a given height error. As done in the previous section, let us indicate with p_S the slave pixel number corresponding to a generic master pixel number p_M, estimated theoretically under the analytical formulation introduced earlier, and assuming that the height of each pixel is exactly known. The relative pixel offset $\Delta p = p_S - p_M$ can be determined through (5) once the slant-range distance between the slave-satellite position and the ground point G, $R_{S,G}$, has been estimated. Since DEM errors δH_G (setting $\tilde{H}_G = H_G + \delta H_G$)

affect the slave slant-range estimation $\tilde{R}_{S,G}$, erroneous values are estimated for the slave pixel number $\tilde{p}_S$ w.r.t. the same master pixel number p_M, and so, for the estimated offset, $\Delta\tilde{p}_{\mathrm{DEM}} = \tilde{p}_S - p_M$, leading to misregistrations $(\Delta\tilde{p}_{\mathrm{DEM}} - \Delta p)$

$$p_S = 2\frac{f_s}{c}R_{S,G} - f_s\tau_{S0} \qquad \tilde{p}_S = 2\frac{f_s}{c}\tilde{R}_{S,G} - f_s\tau_{S0}$$

$$(\Delta\tilde{p}_{\mathrm{DEM}} - \Delta p) = \tilde{p}_S - p_S = 2\frac{f_s}{c}(\tilde{R}_{S,G} - R_{S,G}). \quad (13)$$

Assuming moderate height errors, a linear approximation becomes acceptable, i.e.,

$$\tilde{R}_{S,G} \simeq R_{S,G} + \frac{\partial R_{S,G}}{\partial H_G}\delta H_G$$

$$(\Delta\tilde{p}_{\mathrm{DEM}} - \Delta p) \simeq 2\frac{f_s}{c}\frac{\partial R_{S,G}}{\partial H_G}\delta H_G. \qquad (14)$$

According to the geometrical model described in Section II, the following equation for the slave slant-range variation w.r.t. the topographic height can be derived as

$$\frac{\partial R_{S,G}}{\partial H_G} = \frac{1}{R_{S,G}}\left[(H_G + \rho) - (H_S + \rho)\eta\right] \qquad (15)$$

where

$$\eta = \cos(\delta_{M,G} - \delta_{M,S}) \cdot [1 - \tan\delta_{M,G}$$
$$\times \tan(\delta_{M,G} - \delta_{M,S})\zeta(H_G, H_M, \rho, R_{M,G})] \quad (16)$$

with

$$\zeta(H_G, H_M, \rho, R_{M,G}) = \frac{(H_G + \rho)^2 - \left[(H_M + \rho)^2 - R_{M,G}^2\right]}{(H_G + \rho)^2 - \left[(H_M + \rho) + R_{M,G}\right]^2}$$
$$\cdot \frac{(H_G + \rho)^2 + \left[(H_M + \rho)^2 - R_{M,G}^2\right]}{(H_G + \rho)^2 - \left[(H_M + \rho) - R_{M,G}\right]^2}. \quad (17)$$

This formulation is extendable to the more accurate geometrical model described in Appendix I-A by applying the substitutions in (A3). Moreover, by varying the baseline orientation angle α from $0°$ to $360°$, the influence of DEM errors on the coregistration accuracy may be derived for a range of normal baselines. Fig. 3(c) shows the misregistration trends due to DEM errors in C-, L-, and X-bands w.r.t. the SRTM DEM vertical accuracy and by varying the baseline orientation angle α for a constant topographic height range ΔH_G of 1 km. It can be shown that the influence of H_G in (13)–(16) is very weak. Therefore, a simplified but well-approximated expression for the factor $\zeta(H_G, H_M, \rho, R_{M,G})$ can be retrieved by imposing $H_G = 0$.

In Fig. 3(d). the ratio $(\Delta\tilde{p}_{\mathrm{pol}} - \Delta p)/(\Delta\tilde{p}_{\mathrm{DEM}} - \Delta p)$ is shown for the three bands. The differences among ERS, ALOS, and TerraSAR-X plots in Fig. 3(d) are mainly due to the different look angles, satellite heights, and covered swaths among the sensors. As shown in Fig. 3(d), even with a third-degree polynomial, the misregistrations due to DEM errors are more than ten times less than the pixel-offset residuals due to

the polynomial smoothness. In case of rough topography, we suggest, therefore, a DEM-assisted approach as the preferred method for coregistration of high-resolution images (X-band), as well as for coarser resolution images (L- and C-band). The vertical accuracy of SRTM DEMs can therefore be considered acceptable for a successful DEM-assisted coregistration, still in the case of high-resolution SAR images. It should be noticed that the referred vertical accuracy of SRTM DEMs has to be considered as an optimistic estimate since it refers to a ground resolution much coarser than that of the SAR sensor, even for ERS images (i.e., the SAR images with the worst resolution compared with the other L- or X-band SAR sensors investigated). DEM errors may therefore be much higher in practice, still discarding those introduced by an erroneous DEM radar coding, which are, by themselves, not quite negligible. This means that, particularly for ERS images (where misregistrations due to smooth warp functions are the weakest among the SAR sensors considered in this paper because of the lower range sampling rate), the improvements introduced by the DEM-assisted coregistration may be less significant in practice.

IV. REAL DATA PROCESSING

Recently [19], a first assessment of the potentials of DEM-assisted approach has been carried out by processing real data in the C-, L-, and X-bands. In this section, we illustrate in detail the findings highlighted in the previous section through examples of coregistration of X-band real data, the most affected by local misregistrations even in the case of moderate values for normal baseline and height range in the case of warp functions modeled by polynomials of lower degree.

A. Data-Set Description

Two different test sites have been selected with the purpose of assessing the potentials of the DEM-assisted procedure developed at TU Delft and presently available in the DORIS software [14]. The first one is located in Abruzzo Region, Italy (left of Fig. 5), owing to the availability of five CSK stripmap pairs (Table I) acquired in tandemlike configuration; thus, all span just one day. This ensures low temporal decorrelation, thus allowing the interferometric coherence to be selected as merit figure. Their different normal baselines allow a deeper investigation on the entity of misregistrations in conventional alignment methods when increasing $B_\perp$. The second test site is located in Tanzania (right of Fig. 5), where a pair of TSX stripmap acquisitions (Table I) cover the "Ol Doynio Lengai" Volcano in the Arusha region. The TSX interferogram has a normal baseline higher than the five CSK ones (Table I). The temporal baseline is, in this case of 11 days, coincident with the TSX orbital repeat cycle. Radar-coded SRTM DEMs are shown in Fig. 6 for both test sites. The two test sites have completely different physical settings but similar topographic range ($\sim$2.1 km, Table I), thus allowing further cross comparisons on the performances of both coregistration approaches. Relevant parameters for the CSK and TSX data sets are listed in Table I.
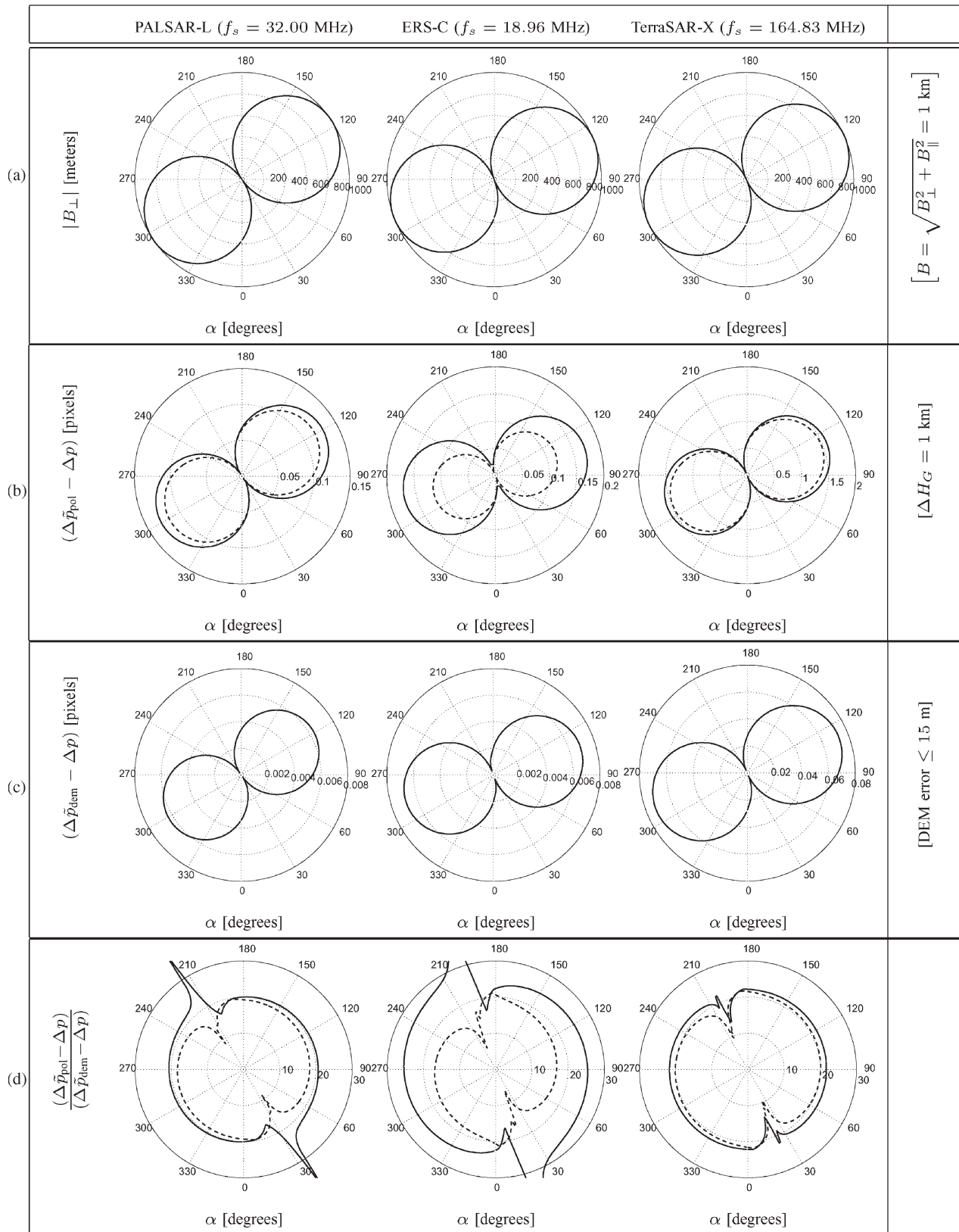
Fig. 3. (a) Polar diagrams of the absolute normal baselines $|B_\perp|$ at midrange for different master–slave configurations obtained by varying the baseline orientation angle α from $0°$ to $360°$ (constant distance $B = 1$ km between master and slave). (b) Polar diagrams of the pixel-offset residuals estimated for (solid line) second- and (dashed line) third-degree polynomial warp functions, corresponding to each pair $(\{\alpha, |B_\perp|\})$ in (a) (the topographic range ΔH_G is assumed to be equal to 1 km). (c) Plots of the pixel-offset residuals due to inaccurate knowledge of the topographic profile by assuming the vertical accuracy of SRTM DEMs. All simulated pixel offsets in (b) and (c) have been derived w.r.t. the look angles of the default stripmap looking modes for ERS/ENVISAT (C-band) and PALSAR (L-band) sensors. Simulations in X-band have been carried out for the specific beam of the TSX real data processed (Table I). (d) Ratio between the pixel-offset residuals due to the smoothness of the polynomial function and the corresponding residuals due to DEM errors. Since, for each pair $(\{\alpha, |B_\perp|\})$, this ratio is much higher than one, the performances of the DEM-A coregistration are always better than the standard approach.
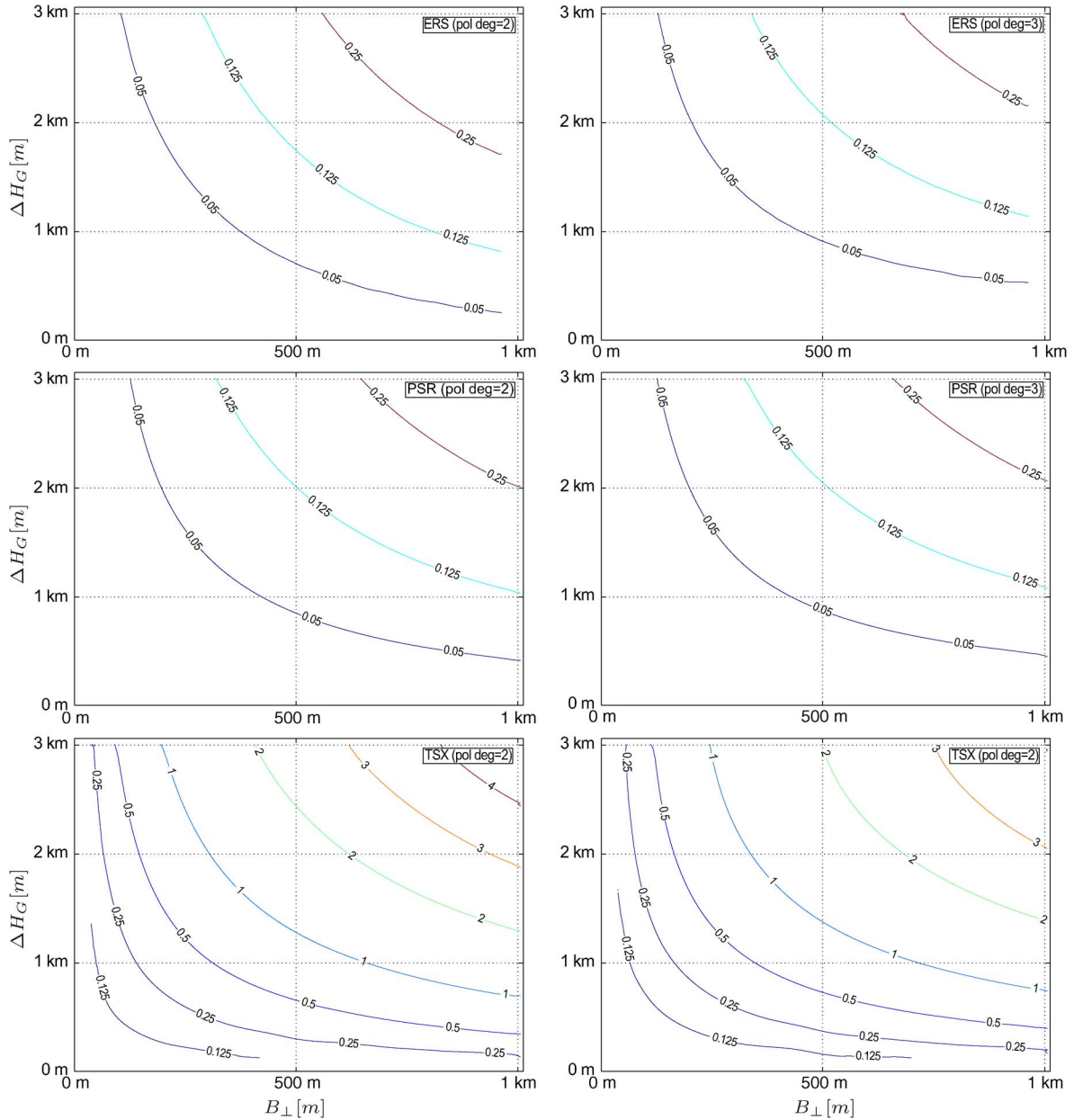
Fig. 4. Diagrams show the entity (in pixels) of range misregistrations estimated for a wide range of normal baselines and topographic ranges in case of warp functions modeled by 2-D polynomial of (left) second and (right) third degree. Top: ENVISAT (swath:IS2)/ERS (C-band); middle: PALSAR (beam:#07—look angle: 34.3°) (L-band); bottom: TerraSAR-X (strip:#05—look angle: 23.9°) (X-band).

B. Methodology

For both the data sets and for all the interferograms in Table I, the assessment of the performances of both the coregistration approaches is performed using two different merit figures, the pixel-offset residuals and the interferometric coherence.

Let us start with the offset-residual computation. First of all, for a high number (over 20 000) of patches (dimension: 128 pixels × 128 lines), pixel offsets between masters and slaves are estimated by maximizing their cross correlation and by discarding patches with a low correlation coefficient (less than 0.4). Second, models for the warp functions that match any pixel of the slaves in the corresponding master geometry are estimated through both conventional and DEM-assisted alignment approaches, as implemented in DORIS. Finally, the

residual pixel offsets along the range directions between the fine offset estimates and the warp models are computed. The processing steps involved in the warp-function estimation for both coregistration approaches can be summarized as follows.

1) *Polynomial warp-function estimation*. 2-D polynomials of low degree (i.e., two for our tests) along the range and azimuth are estimated through Least Mean Squares (LMS) fit over N estimated offset vectors whose correlation is higher than the 0.4 threshold, together with a corresponding w-test statistics estimated on the residual pixel offsets. The procedure is repeated until the w-test statistics along the range and azimuth direction are both lower than a given threshold (1.97 in our case). For each intermediate iteration, the offset vector with the highest
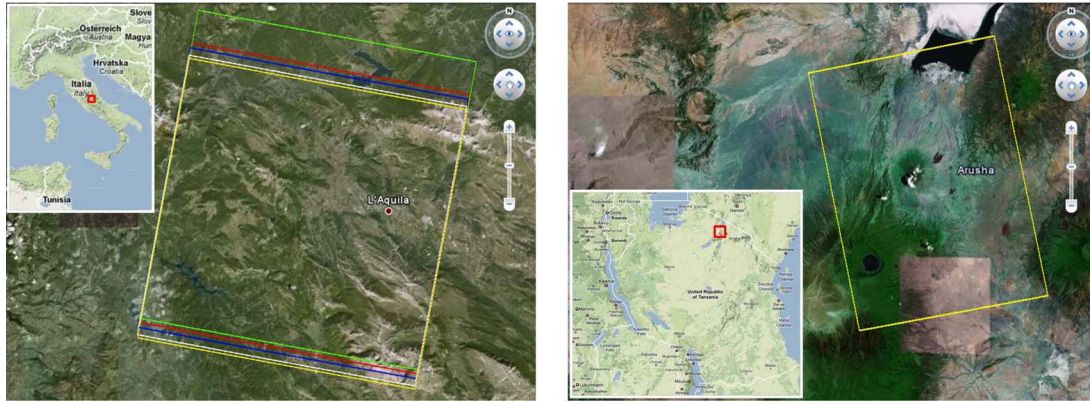
Fig. 5. (Left) Test Site: Abruzzo (Italy). Colored frames refer to the ground coverage of CSK descending interferograms #1 ÷ #5 (see Table I). Inset shows the location of the area of interest (AOI). (Right) Test Site: Ol Doinyo Lengai Volcano (Tanzania). Yellow frame refers to the ground coverage of the TSX ascending interferogram #6 (see Table I). Inset shows the location of the AOI.

TABLE I
PROCESSED STRIPMAP SINGLE-LOOK COMPLEX DATA SET ($B_t \equiv$ Temporal Baseline, $B_\perp \equiv$ Normal Baseline, $B_{\perp,c} \equiv$ Critical Baseline,
$H_M \equiv$ Master Satellite Height, $\Delta H_G \equiv$ Topographic Range Over THE Entire Processed Scene, $\theta_{off} \equiv$ Off−Nadir Angle, $\theta_{inc} \equiv$ Incidence Angle)

TEST SITE	ABRUZZO					OL DOYNIO LENGAI
	(ITALY)					(TANZANIA)
INTERFEROGRAM ID	#1	#2	#3	#4	#5	#6
MASTER SENSOR	CSK-S2	CSK-S2	CSK-S2	CSK-S2	CSK-S2	TSX
SLAVE SENSOR	CSK-S3	CSK-S3	CSK-S3	CSK-S3	CSK-S3	TSX
M [YYYY.MM.DD]	2009.06.06	2009.04.19	2009.05.21	2009.09.10	2009.09.26	2008.05.05
S [YYYY.MM.DD]	2009.06.07	2009.04.20	2009.05.22	2009.09.11	2009.09.27	2008.05.16
FREQUENCY BAND	X (9.60 GHz)	X (9.60 GHz)	X (9.60 GHz)	X (9.60 GHz)	X (9.60 GHz)	X (9.65 GHz)
POLARIZATION	VV	VV	VV	VV	VV	HH
PASS DIRECTION	DESCENDING	DESCENDING	DESCENDING	DESCENDING	DESCENDING	ASCENDING
B_t [days]	1	1	1	1	1	11
$|B_\perp|$ [m]	52	70	148	182	287	313
$|H_{2\pi}|$ [m]	125	92	44	36	23	12
$|B_{\perp,c}|$ [km]	~ 4.98	~ 4.98	~ 4.98	~ 4.98	~ 4.98	~ 4.33
BEAM ID	H4-04	H4-04	H4-04	H4-04	H4-04	STRIP_05
θ_{OFF} [°]	27.71 ÷ 30.47	27.71 ÷ 30.47	27.71 ÷ 30.47	27.71 ÷ 30.47	27.71 ÷ 30.47	~ 23.9
θ_{INC} [°]	30.67 ÷ 33.80	30.67 ÷ 33.80	30.67 ÷ 33.80	30.67 ÷ 33.80	30.67 ÷ 33.80	24.35 ÷ 28.00
RSR [MHz]	127.5	127.5	127.5	127.5	127.5	165
PRF [kHz]	3.33	3.33	3.33	3.33	3.33	3.61
Range BW [MHz]	102.0	102.0	102.0	102.0	102.0	150.0
Azimuth BW [kHz]	2.80	2.80	2.80	2.80	2.80	2.77
Swath Width [km]	~ 41	~ 41	~ 41	~ 41	~ 41	~ 36
H_M [km]	~ 628	~ 628	~ 628	~ 628	~ 628	~ 512
ΔH_G [km]	~ 2.13	~ 2.13	~ 2.13	~ 2.13	~ 2.13	~ 2.13

summed squared w-test statistics is considered as outlier and is then discarded. The 2-D polynomial estimation is hence repeated on the subset of $N-1$ offset vectors, where the detected outlier has been removed. This iterative procedure is repeated until the fit of the polynomial model with the remaining offset vectors is acceptable, i.e., no outliers are detected. Note that an offset vector may be treated as an outlier not only if it has been wrongly

estimated but also in areas with strong topography, in the case the misregistrations due to uncompensated heights exceeds the constraint of $\pm 1/8$ resolution cells required for a proper image alignment.

2) *DEM-assisted coregistration steps.* Offset vectors are computed pixel by pixel by geocoding the master image and applying inverse geocoding procedures to go back in the slave reference geometry, through the use of orbital
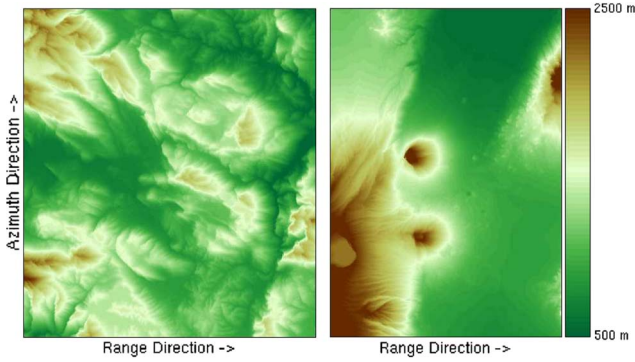
Fig. 6. SRTM DEM radar coded. (Left) Test Site: Abruzzo, Italy (sensor: CSK; pass direction: descending; beam: H4-03). (Right) Test Site: Ol Doinyo Lengai Volcano, Tanzania (sensor: TSX; pass direction: ascending; beam: strip_05).

data and a reference DEM (SRTM-derived). Hence, a first computation of the residual pixel offsets is performed w.r.t. fine offsets estimated through cross correlation between the master and slave. Residual offsets may still be not negligible since the values for the sampling frequency along the slant-range and azimuth direction as well as the fast and slow times of the initial pixel and line, respectively, could be eventually annotated with an inadequate number of significant digits or affected by errors. Hence, an additional LMS fit procedure could be necessary. A 2-D polynomial of the first degree is, in general, sufficient for modeling the mentioned residual offsets. The final warp function is therefore given by the sum of the DEM-assisted model and the 2-D polynomial one, but further on, we refer to it as to the DEM-assisted model, for simplicity.

In the next section, pixel-offset residuals are shown for all the estimated state vectors with a correlation coefficient higher than 0.4. In order to better appreciate the entity of misregistrations in both the coregistration approaches, detected outliers have not been discarded since, as mentioned before, in the case of smooth warp functions, the probability of false alarm in the outlier detection is not negligible.

Regarding the use of the interferometric coherence as merit figure, we recall that the complex coherence γ is defined as [1]

$$\gamma = \frac{E\left[s_1 s_2^*\right]}{\sqrt{E\left[s_1 s_1^*\right]}\sqrt{E\left[s_2 s_2^*\right]}} \qquad (18)$$

where s_1 and s_2 are the two complex SAR signals. Assuming ergodicity, γ can be estimated as

$$\gamma \approx \frac{\langle s_1 s_2^* \exp[-j\phi]\rangle}{\sqrt{\langle s_1 s_1^*\rangle \langle s_2 s_2^*\rangle}} \qquad (19)$$

where the average operation is performed spatially and ϕ is a phase component including effects of topography, displacement, and any other deterministic phase contribution within the estimation window. This spatial estimator is biased for small estimation windows [1]. A spatial dimension of 11×11 pixels is chosen in order to reduce this drawback. It can be shown [20]

that γ can be factorized in terms of the sources of decorrelation as follows:

$$\gamma = \gamma_t \cdot \gamma_g \cdot \gamma_{Dc} \cdot \gamma_{\text{vol}} \cdot \gamma_{\text{thermal}} \cdot \gamma_{\text{proc}} \qquad (20)$$

where the subscripts t, g, Dc, vol, thermal, and proc represent temporal, geometric, Doppler, volume, thermal, and processing decorrelation sources, respectively (see [1] for a detailed description of each contribution). Misregistrations, as well as errors occurring during interpolation, translate in a loss of coherence, expressed by the decorrelation contribution γ_{proc}. Therefore, the estimated coherence can be used to compare the DEM-assisted coregistration potential w.r.t. the standard (polynomial) approach. However, this contribution will be hardly discernible in case the other sources of decorrelation play an important role. Indeed, let us indicate with $\tilde{\gamma}$ (resp., $\hat{\gamma}$) the coherence map evaluated for the interferograms obtained by coregistering the images in the standard way (respectively, through the DEM-assisted procedure). The difference between the coherence maps estimated with the two methodologies is therefore given by

$$\tilde{\gamma} - \hat{\gamma} = \gamma_t \cdot \gamma_g \cdot \gamma_{Dc} \cdot \gamma_{\text{vol}} \cdot \gamma_{\text{thermal}} \cdot (\tilde{\gamma}_{\text{proc}} - \hat{\gamma}_{\text{proc}})$$
$$= \Gamma \cdot (\tilde{\gamma}_{\text{proc}} - \hat{\gamma}_{\text{proc}}). \qquad (21)$$

Our goal is to measure the quantity $(\tilde{\gamma}_{\text{proc}} - \hat{\gamma}_{\text{proc}})$, but this is actually weighted by Γ. A comparison between DEM-assisted and standard coregistration approaches will be more feasible as Γ is close to one. Therefore, only interferograms with the lowest temporal baseline have been generated (one day for CSK-tandem, 11 days for TSX), in order to minimize the temporal decorrelation, as shown in the next section. Moreover, very low coherent areas (i.e., where coherence is less than $\gamma_{\text{th}} = 0.1$) have been masked out when comparing the two alignment approaches. The only drawback of this approach lies on the capability to investigate areas where at least one of the two methods is effective since the areas characterized by strong misregistration are masked out.

C. Results

The CSK data set in Abruzzo consists of five interferometric pairs with normal baselines from few tens of meters up to 287 m (interferograms #1 ÷ #5 in Table I). Range pixel-offset residuals (Fig. 7, at the bottom) confirm the good performances of the DEM-assisted approach since they are confined to a few tenths of pixels regardless of the normal baseline. The standard approach may be considered acceptable only for very low normal baselines, as shown at the top of Fig. 7. In fact, a correlation between the entity of misregistrations and the normal baseline can be noticed, as expected. According to the simulation results (Fig. 4), with a topographic range of around 2 km (as it is for the selected test site), residual offsets overcome 1/8 resolution cell with normal baselines higher than 100 m. This is confirmed by the histograms of the range residual offsets at the top of Fig. 8 relative to the standard approach: the higher the normal baseline is, the higher is the percentage of residual offsets that are worse than a few tenths of pixel. Their spread
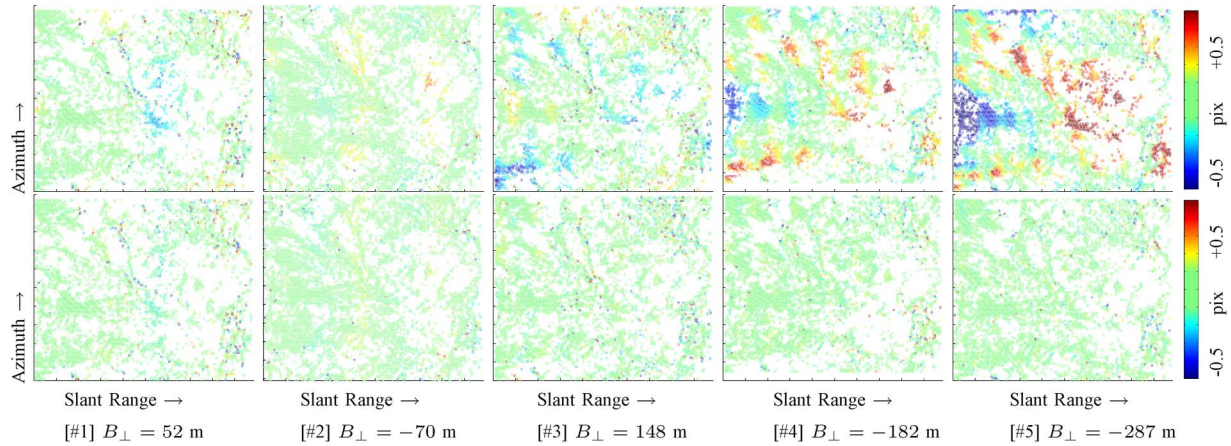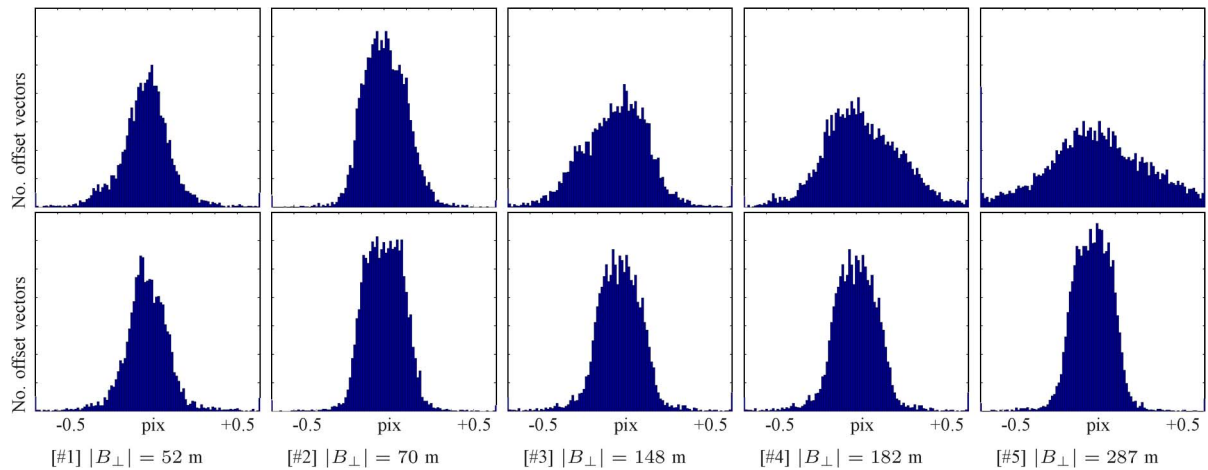
Fig. 7. Test Site: Abruzzo (Italy)—CSK descending data set. Comparison between the range pixel-offset residuals corresponding to (top row) the standard coregistration approach and (bottom row) the DEM-assisted alignment method for interferograms #1 ÷ #5 in Table I (in white, low coherence areas). As expected, maximum residual offsets increase with increasing normal baseline when warp functions are modeled by 2-D polynomials. Indeed, according to simulation results (Fig. 4), with a topographic range of about 2 km (as it is for the selected test site), residual offsets overcome 1/8 resolution cell for normal baselines higher than ~100 m.

Fig. 8. Test Site: Abruzzo (Italy)—CSK descending data set. Histograms of the range pixel-offset residuals for (top row) the standard coregistration approach and for (bottom row) the DEM-assisted alignment method for interferograms #1 ÷ #5 (see Table I). As already seen in Fig. 7, the higher the normal baseline is, the higher is the percentage of residual offsets that is worse than 1/8-resolution cell when warp functions are modeled by polynomials. This percentage becomes unacceptable for normal baselines exceeding ~100 m, according to the simulation results (Fig. 4) with a topographic range of around 2 km (as it is for the selected test site). Instead, residual worsening is not appreciable if a DEM-assisted alignment method is performed.

increases with the normal baseline, while the corresponding histograms for the DEM-assisted alignment, at the bottom in the same figure, are always much more peaked with most of the values well confined in the range of ±1/8 resolution cells, according to the accuracy requirement.

Furthermore, as revealed by the scatterplots of range pixel-offset residuals w.r.t. topographic range for the standard coregistration approach (at the top of Fig. 9), there is an evidence of correlation of residual offsets with topographic range in the case of standard coregistration. No correlation is instead noticeable for the improved DEM-assisted method, as expected (at the bottom in the same figure). It is important to point out that the observed correlation of the polynomial residual offsets is not with the absolute ellipsoid height but with the relative height w.r.t. a mean value over the scene. By comparing the range residual-offset plots at the top of Fig. 7 for the standard coregistration with the radar-coded DEM, shown in Fig. 6 for the selected test site, the residuals appear indeed much more

intense not only at the top of mountainous areas but also on low-laying lands such as valleys, i.e., over all areas whose height is much different from the average value.

Finally, in Fig. 10, the comparison of the performances of the standard coregistration approach versus the DEM-assisted one is accomplished through the interferometric coherence merit figure (resp., γ^s and γ^d) for interferograms #1 ÷ #5 (see Table I). In particular, Fig. 10 has to be interpreted as follows. Low-coherence pixels (where both γ^s and γ^d are lower than a threshold value $\gamma_{th} = 0.1$) have been masked (black color); white dots indicate substantial equivalence in the performances of the two coregistration approaches, i.e., $|\gamma^d - \gamma^s| < \varepsilon$, where ε has been set to 0.05 in order to avoid noise due to the estimator; and red dots indicate better performances of DEM-assisted method w.r.t. the standard one (in other words, $\gamma^d > \gamma^s + \varepsilon$).

The blue dots indicate better performances of the standard coregistration ($\gamma^s > \gamma^d + \varepsilon$): In practice, there is no evidence
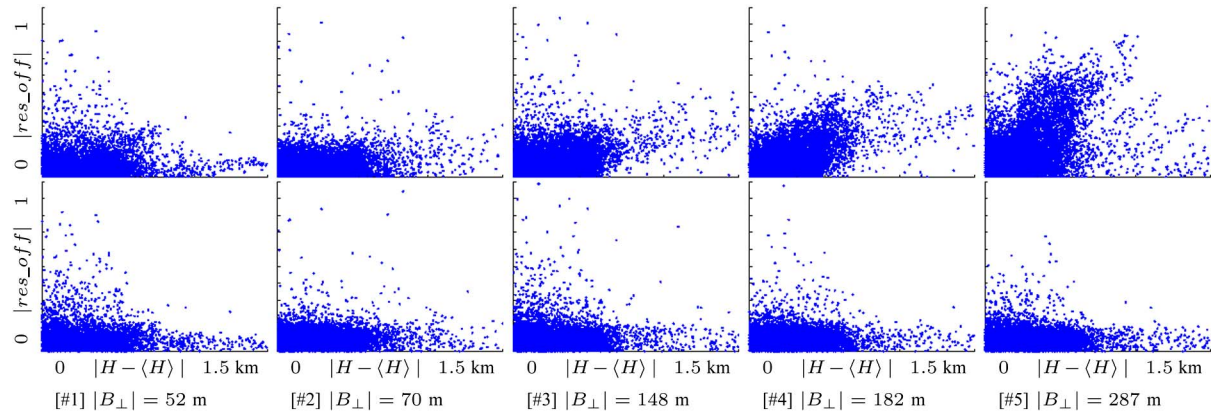
Fig. 9. Test Site: Abruzzo (Italy)—CSK descending data set. Scatterplots of range residual offsets w.r.t. topographic range for (top row) the standard coregistration approach and for (bottom row) the DEM-assisted alignment method for interferograms #1 ÷ #5 (see Table I). The scatterplots reveal correlation of range residual offsets with topographic range in case of standard coregistration, as expected. In particular, by topographic range, we mean here the difference between the actual pixel height and an average height over the selected AOI.
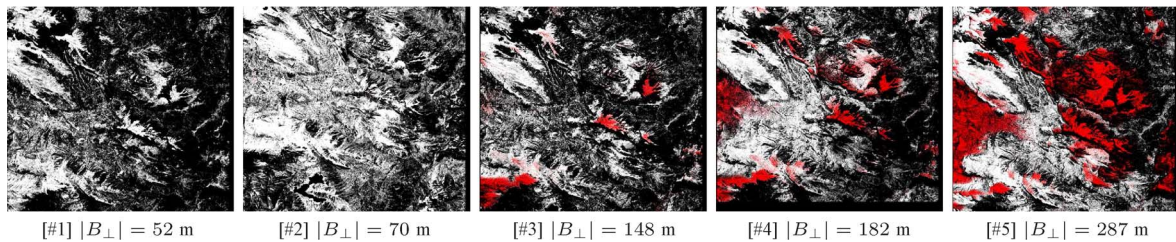
Fig. 10. Test Site: Abruzzo (Italy)—CSK descending data set. Comparison of the performances of the standard coregistration approach versus the DEM-assisted one by comparing the corresponding coherence maps (resp., γ^s and γ^d) for interferograms #1 ÷ #5 (see Table I). Low-coherence pixels (where both γ^s and γ^d are lower than a threshold value $\gamma_{th} = 0.1$) have been masked (black color). White dots indicate substantial equivalence in the performances of the two coregistration approaches $|\gamma^d - \gamma^s| < \varepsilon$, where the threshold ε has been set to 0.05 in order to take into account estimation biases. Red dots indicate better performances of DEM-assisted method w.r.t. the standard one (in other words, $\gamma^d > \gamma^s + \varepsilon$). Blue dots show better performances of the standard coregistration $(\gamma^s > \gamma^d + \varepsilon)$. Note the consistently better performance of DEM-assisted coregistration w.r.t. the standard approach. The higher the normal baseline is, the higher is the difference in the effectiveness of the two coregistration approaches, also in terms of processing decorrelation and overall interferometric coherence.

of better performances of standard coregistration in any of the interferograms analyzed. The interferometric coherence confirms therefore the conclusions drawn from the analysis of the first merit figure: the higher the normal baseline is, the higher is the gain in performance introduced by the DEM-assisted approach. Let us consider now the second (Tanzania) test site and the TSX ascending interferogram, labeled as #6 in Table I. Identical conclusions may be drawn for it in terms of pixel-offset residuals (Figs. 11 and 12) and their correlation to topography (Fig. 13). The longer baseline (> 300 m, Table I) leads to residual offsets exceeding one pixel when warp functions are modeled by 2-D polynomials, in accordance with simulation results (Fig. 4). In this case study, the improvement in interferometric coherence is clearly visible at the top of the Ol Doinyo Lengai Volcano (Fig. 14), where the coherence maps corresponding to both the coregistration approaches are shown for a visual comparison. There is no evidence of better performances of standard coregistration even in the coherence difference map shown in Fig. 15.

Real-data-processing results confirm therefore that the DEM-assisted approach to SAR image alignment is generally worthwhile for the case of high-resolution SAR data and justifies the higher computational cost. In those cases in which the standard coregistration is still acceptable, i.e., for short baselines, the DEM-assisted approach never shows worse performances.
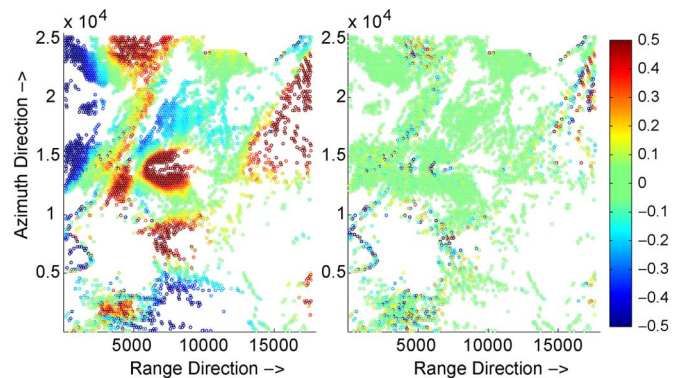

Fig. 11. Test Site: Ol Doinyo Lengai (Tanzania). Range pixel-offset residuals for the TSX ascending interferogram #6 (see Table I). (Left) Standard coregistration. (Right) DEM-assisted coregistration (in white, low-coherence areas). According to simulation results (Fig. 4), with a topographic range of around 2 km (as it is for the selected test site), residual offsets overcome one pixel with normal baselines higher than 300 m when warp functions are modeled by 2-D polynomials.

V. CONCLUSION

An assessment of the performances of a geometrical DEM-assisted coregistration w.r.t. more traditional approaches (warp functions modeled as 2-D polynomials) has been carried out. In particular, the impact of range sampling rate, topographic
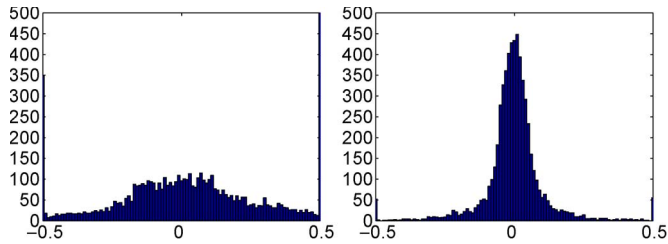
Fig. 12. Test Site: Ol Doinyo Lengai Volcano (Tanzania). Histograms of the residual offsets along the slant range for the TSX ascending interferogram #6 ($B_\perp \approx 313$ m, see Table I). (Left) Standard coregistration. (Right) DEM-assisted coregistration. The percentage of residual offsets that is worse than 1/8 resolution cell is unacceptable when warp functions are modeled by polynomials.
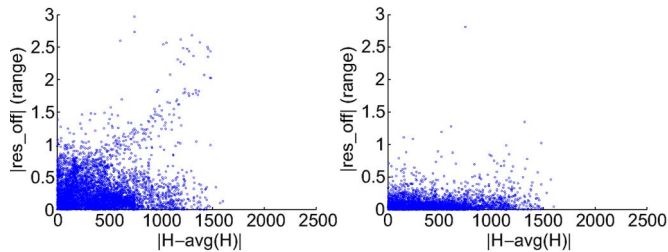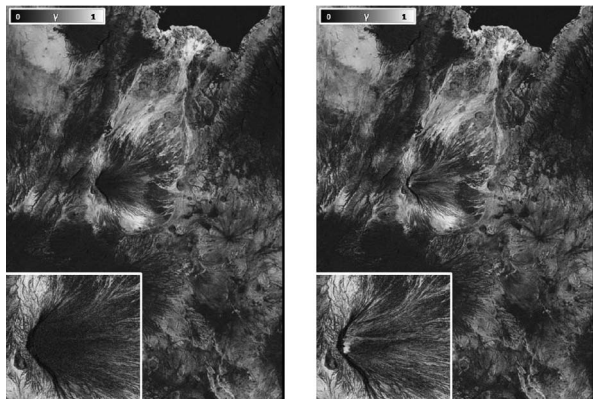

Fig. 13. Test Site: Ol Doinyo Lengai Volcano (Tanzania). Scatterplots of range residual offsets w.r.t. topographic range for (top images) the standard coregistration approach and for (bottom images) the DEM-assisted alignment method for TSX interferogram #6 (see Table I). Scatterplots reveal correlation of residual offsets with topographic range in the case of standard coregistration, as expected. In particular, by topographic range, we mean here the difference between the actual pixel height and an average height over the selected AOI.

Fig. 14. Test Site: Ol Doinyo Lengai Volcano (Tanzania). Coherence maps estimated for the TSX ascending interferogram #6 ($B_\perp \approx 313$ m, see Table I) when master and slave images are coregistered through (left) conventional method and (right) DEM-assisted approach. The improvement in the coherence is clearly visible at the top of the volcano.

Fig. 15. Test Site: Ol Doinyo Lengai Volcano (Tanzania)—TSX ascending interferogram #6 ($B_\perp \approx 313$ m, see Table I). Comparison of the performances of the standard coregistration approach versus the DEM-assisted one is accomplished here by comparing the corresponding coherence maps (resp., γ^s and γ^d). (Black color) Low-coherence pixels (where both γ^s and γ^d are lower than a threshold value $\gamma_{th} = 0.1$) have been masked. White dots indicate substantial equivalence in the performances of the two coregistration approaches $|\gamma^d - \gamma^s| < \varepsilon$, where ε has been set to 0.05 in order to take into account estimation biases. Red dots indicate better performances of DEM-assisted method w.r.t. standard one (in other words, $\gamma^d > \gamma^s + \varepsilon$). Blue dots show better performances of the standard coregistration ($\gamma^s > \gamma^d + \varepsilon$): Again, there is no evidence of better performances of standard coregistration.

mance diagrams have been drawn from the simulation results, which may be used as quick reference to decide case by case whether the DEM-assisted method is really necessary in order to ensure subpixel alignment accuracy. The two coregistration approaches have been further compared by processing real data acquired by the CSK and TSX missions since, among the three radar bands, X-band is most affected by misregistrations due to uncompensated topography. Coregistration tests on real data have been carried out by applying conventional and DEM-assisted methods implemented in the DORIS open-source SAR interferometric processing tool developed at TU Delft. Real data processing confirms that 1) conventional alignment methods become inaccurate when dealing with higher resolution data as soon as the normal baseline or the topographic range increases and 2) good performances of the DORIS processing chain are obtained for the coregistration of high-resolution SAR data.

APPENDIX I

A. Geometric Model Refinement

The model introduced in Section II approximates the reference ellipsoid with a sphere tangent to it in the point P_M^{nad} (Fig. 1), i.e., the nadir projection of the master-satellite position on the reference ellipsoid. The radius ρ of the spherical model is coincident with the Earth curvature radius R_{az} in P_M^{nad} in the zero-Doppler plane π. The validity of the model so far introduced relies on the assumption that, for every point along the ground swath, the difference between the heights above the spherical approximation just defined H_G and the reference ellipsoid h_G may be considered negligible (Fig. 1). In other words, it assumes implicitly that the curvature center of the elliptic cross section in the zero-Doppler plane π corresponding to a point generically selected along the swath extension is

range over the covered swath, and DEM errors on the final coregistration precision has been evaluated for different radar wavelenghts, postings, and side-looking geometries through both analytical relationships and simulations. Simulation tests show that DEM-assisted coregistration is recommended, particularly in the case of long normal baselines and rough topography. In particular, for X-band interferometry, this approach is absolutely preferable to the standard one, in spite of its higher computational cost, because of the higher resolution of the data w.r.t. C- and L-bands. The entity of misregistrations due to smooth warp functions (such as 2-D polynomials) has been theoretically estimated for all the three radar bands for a wide range of normal baselines and topographic ranges. Perfor-
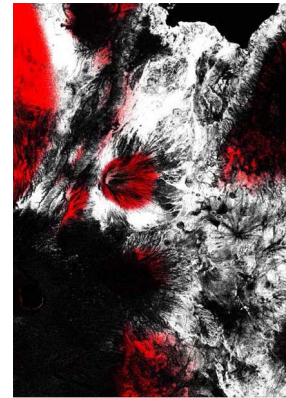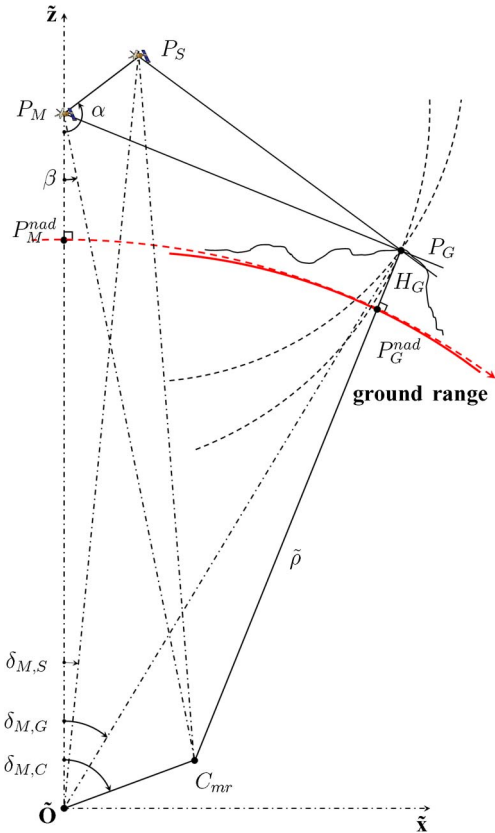
Fig. 16.   Refined geometric model. The elliptic cross section (dashed red line) between the reference ellipsoid (WGS84) and the zero-Doppler plane π is approximated with (solid red line) a circle centered in C_{mr}, i.e., the curvature center of the ellipse w.r.t. the nadir projection of the point $P_{G,\mathrm{mr}}$, located at midrange $\tilde{O}$, the curvature center of the ellipse w.r.t. the nadir projection P_M^{nad} of the master satellite position. The position of the slave satellite is provided in terms of the distance B (or baseline) and the baseline orientation angle α measured from the master nadir-direction toward its looking direction.

coincident or, at least, very close to the origin $\tilde{O}$, i.e., the curvature center w.r.t. the nadir projection of the master satellite position P_M^{nad}. This approximation is acceptable only for very low geodetic latitudes (e.g., Tanzania—see Section IV-A) since, near the Equator, the orbital heading α_h is not too far from $0°$ or $180°$ (depending on the orbital-pass direction, whether ascending or descending), and therefore, the zero-Doppler plane π is roughly parallel to the prime vertical section. Since, for any point located near to Equator, its prime vertical section is, in turn, roughly parallel to the equatorial plane, the eccentricity of the corresponding elliptic cross section is very close to one. For high latitudes, however, a model refinement is necessary. In this case, indeed, by evaluating the distance between a generic ground point and the origin $\tilde{O}$, its variation along a swath extension of 100 km (ERS) may also reach hundreds of meters. In these cases, the origin $\tilde{O}$ cannot be considered anymore close to the center of the curvature of the elliptic cross section along the swath width, and a refinement of the spherical model is necessary (Fig. 16). Because of the side-looking acquisition geometry, this can be obtained by substituting the projection circle π with a circle whose center C_{mr} and radius $\tilde{\rho}$ are equal, respectively, to the center and radius of curvature of the elliptic cross section corresponding to the point $P_{\mathrm{mr}}^{\mathrm{nad}}$ located at swath middle range, instead of the master nadir projection P_M^{nad}

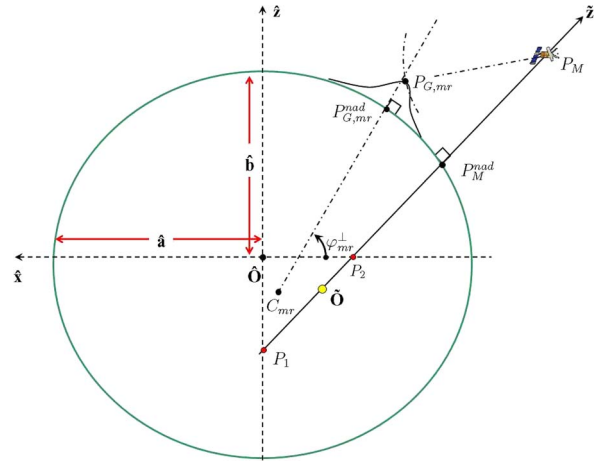Fig. 17.   Two-dimensional view of the elliptic cross section of the reference ellipsoid on the zero-Doppler plane π. $\tilde{O}$ and C_{mr} are the curvature centers in the nadir projections P_M^{nad} and $P_{\mathrm{mr}}^{\mathrm{nad}}$ of the master-satellite position and the ground point at middle range, respectively. In practice, $\tilde{O}$ is always located between points P_1 (center of curvature of the prime vertical in P_M^{nad}) and P_2, depending on the particular azimuth angle of the section π. See also Fig. 2 for the location of points P_1 and P_2.

(see Fig. 17). Simulations show that this approximation is valid at any latitude since the distance between a generic point on the ellipse and the curvature center C_{mr} differs from the radius $\tilde{\rho}$ by no more than half centimeter within a 100-km swath extension and slightly higher for a 250-km swath. The model is also valid for wider swaths, such as in the case of the future Sentinel-1 mission ($\sim$250 km) for the Interferometric Wide Swath Mode. The position of the center C_{mr} can be easily derived once an analytical expression for the elliptic cross section in the zero-Doppler plane π has been retrieved. With respect to the $\tilde{O}\tilde{x}\tilde{z}$ reference system, this elliptic cross section (whose semi-axes $\hat{a}$ and $\hat{b}$ and first eccentricity $\hat{e}$ are different, in general, from those of the reference ellipsoid) is described by the following:

$$\frac{(r_{x\tilde{x}}\tilde{x} + r_{x\tilde{z}}\tilde{z} + x_{\tilde{O}})^2}{a^2} + \frac{(r_{y\tilde{x}}\tilde{x} + r_{y\tilde{z}}\tilde{z} + y_{\tilde{O}})^2}{a^2}$$
$$+ \frac{(r_{z\tilde{x}}\tilde{x} + r_{z\tilde{z}}\tilde{z} + z_{\tilde{O}})^2}{b^2} = 1 \quad \text{(A1)}$$

where the coefficients $r_{i\tilde{j}}$ are given by (4).

Once a rotation and translation of the $\tilde{O}\tilde{x}\tilde{z}$ axes are performed in order to make them coincident with the ellipse axes (coordinate system $\hat{O}\hat{x}\hat{z}$ in Fig. 17), the coordinates of the curvature center C_{mr} are given by

$$\hat{x}_{C_{\mathrm{mr}}} = \hat{x}_{P_{\mathrm{mr}}^{\mathrm{nad}}} - \frac{\hat{a}(1 - \hat{e}^2)\cos\varphi_{P_{\mathrm{mr}}^{\mathrm{nad}}}}{\sqrt[3]{1 - \hat{e}^2\sin^2\varphi_{P_{\mathrm{mr}}^{\mathrm{nad}}}}}$$

$$\hat{y}_{C_{\mathrm{mr}}} = \hat{y}_{P_{\mathrm{mr}}^{\mathrm{nad}}} - \frac{\hat{a}(1 - \hat{e}^2)\sin\varphi_{P_{\mathrm{mr}}^{\mathrm{nad}}}}{\sqrt[3]{1 - \hat{e}^2\sin^2\varphi_{P_{\mathrm{mr}}^{\mathrm{nad}}}}} \quad \text{(A2)}$$

where $P_{\mathrm{mr}}^{\mathrm{nad}}$ is the projection on the ellipse of the ground point at middle range G_{mr}, and the angle $\varphi_{P_{\mathrm{mr}}^{\mathrm{nad}}}$ (Fig. 17) should not be confused with the geodetic latitude of $P_{\mathrm{mr}}^{\mathrm{nad}}$ since the

zero-Doppler plane π is not coincident, in general, with the prime-meridian section.

As before, our aim is to estimate, for each master pixel p_M, the corresponding range pixel offset between master and slave or, equivalently [see (7)], the distance $R_{S,G}$ between the slave satellite and the ground point G. Assuming that the position of C_{mr} in the $\tilde{O}\tilde{x}\tilde{z}$ reference system has been retrieved for a generic master slow time, the distance $R_{S,G}$ can be estimated more accurately in the refined geometrical model just described. It can be shown that (9) is still valid provided the following substitutions are made:

$$\alpha \to (\alpha - \beta),$$
$$(\rho + H_M) \to R_{C,M},$$
$$(\rho + H_S) \to R_{C,S},$$
$$(\rho + H_G) \to (\tilde{\rho} + H_G) \tag{A3}$$

where the height H_G above the spherical model for a generic point G along the swath extension may be further replaced with the corresponding value h_G above the reference ellipsoid, which is a quantity easily retrieved from any DEM due to the refined spherical model described in this section, and

$$R_{C,M} = \sqrt{R_{\tilde{O},M}^2 + R_{\tilde{O},C}^2 - 2R_{\tilde{O},M}R_{\tilde{O},C}\cos\delta_{M,C}}$$
$$R_{C,S} = \sqrt{R_{\tilde{O},S}^2 + R_{\tilde{O},C}^2 - 2R_{\tilde{O},S}R_{\tilde{O},C}\cos(\delta_{M,C} - \delta_{M,S})}$$
$$R_{\tilde{O},S} = \sqrt{R_{\tilde{O},M}^2 + B^2 - 2BR_{\tilde{O},M}\cos\alpha}$$
$$\sin\beta = \frac{R_{\tilde{O},C}}{R_{C,M}}\sin\delta_{M,C}$$
$$\sin\delta_{M,S} = \frac{B}{R_{\tilde{O},S}}\sin\alpha \tag{A4}$$

are all known quantities not dependent on the master pixel considered. In conclusion, the spherical model defined by (9) can still be considered a good approximation of the ellipsoid surface along the ground swath for high latitudes provided the substitutions listed in (9) are made.

B. Analytical Derivation of the Coregistration Sensitivity to DEM Vertical Accuracy

Let us assume to coregister SAR images through a DEM-assisted approach. In this section, we derive analytically the entity of range pixel-offset residuals for a given height error due, for example, to the intrinsic finite vertical accuracy of the DEM or to inaccurate radar-coding procedures.

As mentioned in Section III-B, a good approximation for the entity of the misregistration $(\Delta\tilde{p}_{\mathrm{DEM}} - \Delta p)$ for a given height error δH_G is provided by (14). According to the geometrical model described in Section II, the entity of the misregistration due to a given radar-coded height error can therefore be easily estimated once the slave slant-range variation w.r.t. the topographic height is known along the swath width. In this section,

such expression is analytically derived. The slave slant range may be written as (Fig. 1)

$$R_{S,G} = \left[(H_S + \rho)^2 + (H_G + \rho)^2 \right.$$
$$\left. - 2(H_S + \rho)(H_G + \rho)\cos\delta_{S,G}\right]^{\frac{1}{2}}. \tag{B1}$$

Therefore, its variation with the topographic height is given by

$$\frac{\partial R_{S,G}}{\partial H_G} = \frac{1}{R_{S,G}}\left[(H_G + \rho) - (H_S + \rho)\cos\delta_{S,G} \right.$$
$$\left. + (H_S + \rho)(H_G + \rho)\sin\delta_{S,G}\frac{\partial\delta_{S,G}}{\partial H_G}\right]. \tag{B2}$$

Let us compute therefore the variation of the angle $\delta_{S,G}$ with the topographic height (Fig. 1). From (8)

$$\delta_{S,G} = \delta_{M,G} - \arcsin\frac{B\sin\alpha}{(H_S + \rho)}. \tag{B3}$$

Hence

$$\frac{\partial\delta_{S,G}}{\partial H_G} = \frac{\partial\delta_{M,G}}{\partial H_G}. \tag{B4}$$

Therefore, let us derive analytically the angle $\delta_{M,G}$ and its variation with H_G

$$\delta_{M,G} = \arcsin\left(\frac{R_{M,G}}{H_G + \rho}\sin\theta_M\right)$$
$$= \arcsin(f(H_G)) \tag{B5}$$
$$\frac{\partial\delta_{M,G}}{\partial H_G} = \frac{1}{\cos\delta_{M,G}}\frac{\partial f(H_G)}{\partial H_G} \tag{B6}$$

since the master look angle for the generic pixel p_M is a function only of the corresponding ellipsoid height H_G, once fixed to the side-looking geometry

$$\cos\theta_M = \frac{\left[(H_M + \rho)^2 + R_{M,G}^2 - (H_G + \rho)^2\right]}{2R_{M,G}(H_M + \rho)}. \tag{B7}$$

Finally, let us compute the function f, just introduced, and its first derivative

$$f(H_G) = \frac{R_{M,G}}{H_G + \rho}$$
$$\cdot \sqrt{1 - \frac{\left[(H_M + \rho)^2 + R_{M,G}^2 - (H_G + \rho)^2\right]^2}{4R_{M,G}^2(H_M + \rho)^2}}$$
$$= \frac{\sqrt{\xi}}{2(H_M + \rho)(H_G + \rho)} \tag{B8}$$

where

$$\xi = \left[(H_M + \rho + R_{M,G})^2 - (H_G + \rho)^2\right]$$
$$\cdot \left[(H_G + \rho)^2 - (H_M + \rho - R_{M,G})^2\right]. \tag{B9}$$

Thus

$$
\frac{\partial f(H_G)}{\partial H_G} = \frac{1}{2(H_M+\rho)}\left[\frac{-\sqrt{\xi}}{(H_G+\rho)^2} + \frac{1}{2(H_G+\rho)\sqrt{\xi}} \cdot \frac{\partial \xi}{\partial H_G}\right]
$$

$$
= \sin\delta_{M,G}\left[-\frac{1}{(H_G+\rho)} + \frac{1}{2\xi}\cdot\frac{\partial\xi}{\partial H_G}\right] \quad \text{(B10)}
$$

where

$$
\frac{\partial\xi}{\partial H_G} = -2(H_G+\rho)
$$

$$
\times \left\{\left[(H_G+\rho)^2 - (H_M+\rho-R_{M,G})^2\right]\right.
$$

$$
\left. - \left[(H_M+\rho+R_{M,G})^2 - (H_G+\rho)^2\right]\right\}
$$

$$
= -4(H_G+\rho)\left\{(H_G+\rho)^2 - (H_M+\rho)^2 - R_{M,G}^2\right\}.
$$
$$\text{(B11)}$$

Hence

$$
\frac{\partial f(H_G)}{\partial H_G} = \sin\delta_{M,G}\left\{-\frac{1}{(H_G+\rho)} - \frac{2(H_G+\rho)^3}{\xi}\right.
$$

$$
\left. + \frac{2(H_G+\rho)\left[(H_M+\rho)^2 + R_{M,G}^2\right]}{\xi}\right\}
$$

$$
= -\frac{\sin\delta_{M,G}}{(H_G+\rho)}[1+\Omega] \quad \text{(B12)}
$$

where

$$
1+\Omega = 1 + \frac{2(H_G+\rho)^2}{[(H_M+\rho+R_{M,G})^2 - (H_G+\rho)^2]}
$$

$$
\cdot \frac{\left[(H_G+\rho)^2 - (H_M+\rho)^2 - R_{M,G}^2\right]}{[(H_G+\rho)^2 - (H_M+\rho-R_{M,G})^2]}
$$

$$
= -\frac{\left[(H_G+\rho)^2 - ((H_M+\rho)^2 - R_{M,G}^2)\right]}{\left[(H_G+\rho)^2 - ((H_M+\rho)+R_{M,G})^2\right]}
$$

$$
\cdot \frac{\left[(H_G+\rho)^2 + ((H_M+\rho)^2 - R_{M,G}^2)\right]}{\left[(H_G+\rho)^2 - ((H_M+\rho)-R_{M,G})^2\right]}. \quad \text{(B13)}
$$

Summarizing, we have

$$
\frac{\partial R_{S,G}}{\partial H_G} = \frac{1}{R_{S,G}}\left[(H_G+\rho) - (H_S+\rho)\cos\delta_{S,G}\right.
$$

$$
\left. + (H_S+\rho)(H_G+\rho)\sin\delta_{S,G}\frac{\partial\delta_{S,G}}{\partial H_G}\right]
$$

$$
= \frac{1}{R_{S,G}}\left[(H_G+\rho) - (H_S+\rho)\cos\delta_{S,G}\right.
$$

$$
\left. + (H_S+\rho)(H_G+\rho)\frac{\sin\delta_{S,G}}{\cos\delta_{M,G}}\frac{\partial f_G}{\partial H_G}\right]
$$

$$
= \frac{1}{R_{S,G}}\left[(H_G+\rho) - (H_S+\rho)\eta\right] \quad \text{(B14)}
$$

where

$$
\eta = \cos(\delta_{M,G} - \delta_{M,S}) \cdot [1 - \tan\delta_{M,G}
$$

$$
\times \tan(\delta_{M,G} - \delta_{M,S})\zeta(H_G, H_M, \rho, R_{M,G})] \quad \text{(B15)}
$$

with

$$
\zeta(H_G, H_M, \rho, R_{M,G})
$$

$$
= \frac{(H_G+\rho)^2 - \left[(H_M+\rho)^2 - R_{M,G}^2\right]}{(H_G+\rho)^2 - \left[(H_M+\rho)+R_{M,G}\right]^2}
$$

$$
\cdot \frac{(H_G+\rho)^2 + \left[(H_M+\rho)^2 - R_{M,G}^2\right]}{(H_G+\rho)^2 - \left[(H_M+\rho)-R_{M,G}\right]^2}. \quad \text{(B16)}
$$

End of proof.

REFERENCES

[1] R. F. Hanssen, *Radar Interferometry: Data Interpretation and Error Analysis*. Dordrecht, The Netherlands: Kluwer, 2001.
[2] P. Coppin, I. Jonckheere, K. Nackaerts, B. Muys, and E. Lambin, "Digital change detection methods in ecosystem monitoring: A review," *Int. J. Remote Sens.*, vol. 25, no. 9, pp. 1565–1596, May 2004.
[3] P. A. van den Elsen, E.-J. D. Pol, and M. A. Viergever, "Medical image matching—A review with classification," *IEEE Eng. Med. Biol. Mag.*, vol. 12, no. 1, pp. 26–39, Mar. 1993.
[4] B. Zitova and J. Flusser, "Image registration methods: A survey," *Image Vis. Comput.*, vol. 21, no. 11, pp. 977–1000, Oct. 2003.
[5] F. W. Leberl, *Radargrammetric Image Processing*, 1st ed. Norwood, MA: Artech House, 1990.
[6] A. Refice, F. Bovenga, and R. Nutricato, "MST-based stepwise connection strategies for multi-pass radar data, with application to coregistration and equalization," *IEEE Trans. Geosci. Remote Sens.*, vol. 44, no. 8, pp. 2029–2040, Aug. 2006.
[7] P. Marinkovic and R. F. Hanssen, "Advanced InSAR coregistration using point clusters," in *Proc. ENVISAT ERS Symp.*, Salzburg, Austria, Sep. 2004.
[8] F. Serafino, "SAR image coregistration based on isolated point scatterers," *IEEE Geosci. Remote Sens. Lett.*, vol. 3, no. 3, pp. 354–358, Jul. 2006.
[9] G. Fornaro and G. Franceschetti, "Image registration in interferometric SAR processing," *Proc. Inst. Elect. Eng.—Radar, Sonar, Navig.*, vol. 142, no. 6, pp. 313–320, Dec. 1995.
[10] R. Scheiber and A. Moreira, "Coregistration of interferometric SAR images using spectral diversity," *IEEE Trans. Geosci. Remote Sens.*, vol. 38, no. 5, pp. 2179–2191, Sep. 2000.
[11] E. Sansosti, P. Berardino, M. Manunta, F. Serafino, and G. Fornaro, "Geometrical SAR image registration," *IEEE Trans. Geosci. Remote Sens.*, vol. 44, no. 10, pp. 2861–2870, Oct. 2006.
[12] M. Arikan, F. van Leijen, L. Guang, and R. F. Hanssen, "Improved image alignment under the influence of elevation," in *Proc. FRINGE*, 2007. [CD-ROM].

[13] M. Eineder, N. Adam, and N. Yague-Martinez, "First TerraSAR-X interferometry evaluation," in *Proc. FRINGE*, 2007. [CD-ROM].

[14] B. M. Kampes, R. F. Hanssen, and Z. Perski, "Radar interferometry with public domain tools," in *Proc. FRINGE*, 2003. [CD-ROM].

[15] Y. Huanyin, R. Hanssen, J. Kianicka, P. Marinkovic, F. van Leijen, and G. Ketelaar, "Sensitivity of topography on InSAR data coregistration," in *Proc. Envisat ERS Symp.*, 2004. [CD-ROM].

[16] L. Euler, "Recherches sur la courbure des surfaces," *Mémoires de l'academie des sciences de Berlin*, vol. 16, pp. 119–143, 1767.

[17] J. Meusnier, "Mémoire sur la courbure des surfaces," *Mémoires des savans étrangers*, vol. 10, pp. 477–510, 1785.

[18] D. O. Nitti, L. D. Vitis, F. Bovenga, R. Nutricato, A. Refice, and J. Wasowski, "Multi-temporal L-band SAR interferometry confirms C-band spatial patterns of subsidence in the ancient Wieliczka Salt Mine (UNESCO Heritage Site, Poland)," in *Proc. FRINGE*, 2009. [CD-ROM].

[19] D. O. Nitti, R. F. Hanssen, A. Refice, F. Bovenga, G. Milillo, and R. Nutricato, "Evaluation of DEM-assisted SAR coregistration," *Proc. SPIE*, vol. 7109, pp. 710 919-1–710 919-14, 2008. DOI: 10.1117/12.802767.

[20] H. A. Zebker and J. Villasenor, "Decorrelation in interferometric radar echoes," *IEEE Trans. Geosci. Remote Sens.*, vol. 30, no. 5, pp. 950–959, Sep. 1992.

Davide Oscar Nitti received the Laurea (*cum laude*) degree in electronic engineering from the Politecnico di Bari, Bari, Italy, in 2006 and the Ph.D. degree in engineering and chemistry for ecosystems conservation from the Italian Interpolitechnic School of Doctorate in 2010.

In February 2008, he was with the research group of Prof. R. F. Hanssen at Delft University of Technology, Delft, The Netherlands, where he worked for nine months on L- and X-band synthetic aperture radar (SAR) interferometry. He is currently a Contract Researcher with Politecnico di Bari. His main interests concern environmental risk assessment and geohazards monitoring through multitemporal SAR interferometry.

Ramon F. Hanssen (M'04) received the M.Sc. degree in geodetic engineering and the Ph.D. (*cum laude*) degree from the Delft University of Technology, Delft, The Netherlands, in 1993 and 2001, respectively.

He was with the International Institute for Aerospace Survey and Earth Science (ITC), Stuttgart University, Stuttgart, Germany; the German Aerospace Center (DLR); Stanford University, Stanford, CA (Fulbright Fellow); and Scripps Institution of Oceanography in the field of microwave remote sensing, radar interferometry, signal processing and geophysical application development. Since 2008, he has been an Antoni van Leeuwenhoek Professor in Earth observation with the Delft University of Technology, where, since 2009, he has been leading the research group on mathematical geodesy and positioning. He is the author of a textbook on radar interferometry.

Alberto Refice received the Laurea (*cum laude*) degree and the Ph.D. degree in physics from the University of Bari, Bari, Italy, in 1994 and 1998, respectively.

He was with the University of Bari as a Postdoctoral Fellow and Contract Researcher from 1998 to 2001. Since 2001, he has been with Consiglio Nazionale delle Ricerche-Istituto di Studi sui Sistemi Intelligenti per l'Automazione (CNR-ISSIA) as a Researcher. He is involved in several research projects sponsored by the European Space Agency, European Union (UE), Italian Space Agency (ASI), and other local Italian institutions, and has coauthored more than 50 journal papers and conference communications. He is working on various aspects of the development of point-target processing techniques for differential synthetic aperture radar (SAR) interferometry, aimed at displacement monitoring, as well as innovative wideband multichromatic SAR data-processing approaches. His main interests concern advanced processing techniques for remote-sensing data, particularly radar interferometry, and their applications to the retrieval of geobiophysical parameters.

Fabio Bovenga received the Laurea degree and the Ph.D. degree in physics from the University of Bari, Bari, Italy, in 1997 and 2005, respectively.

He was with the University of Bari. Since 2007, he has been with the Italian Research Council, where he is currently a Researcher with the Istituto di Studi sui Sistemi Intelligenti per l'Automazione (ISSIA), Bari. He participated in many scientific projects funded by national and international space agencies (Italian Space Agency/European Space Agency/National Aeronautics and Space Administration) as well as by the European Union and has tens of publications on both international journals and conference proceeding. He is also involved in the exploitation of new generation of wideband synthetic aperture radar (SAR) data, and he had designed and developed the innovative algorithm of multichromatic analysis of SAR interferometry data for height retrieval. His main interests concern advanced processing techniques for SAR imaging and radar interferometry and the application of multipass interferometry analysis to ground-instability monitoring and modeling.

Raffaele Nutricato received the Laurea (*cum laude*) degree in electronic engineering from the Politecnico di Bari, Bari, Italy, in 2001.

From 2001 to 2008, he has been with Politecnico di Bari as a Contract Researcher. He has participated in many scientific projects funded by national and international space agencies (Italian Space Agency/European Space Agency/National Aeronautics and Space Administration) and by the European Union. Since 2004, he has also been with ATMEL Corporation, Rome, Italy as a Consultant in the development of audio applications implemented on digital signal processor devices. Since 2008, he has been with Geophysical Applications Processing s.r.l., Bari, Italy, as Technical Manager. His main research interests concern advanced processing techniques for synthetic aperture radar imaging and radar interferometry and the application of multitemporal interferometric analysis to slope/building instability monitoring.

Correspondence

Corrections to "Impact of DEM-Assisted Coregistration on High-Resolution SAR Interferometry"

Dong Li, *Student Member, IEEE*, and Yunhua Zhang, *Member, IEEE*

The last expression of equation (8) in [1] is incorrect. According to the cosine law, the correct expression should be

$$\cos \theta_{\sigma,G} = \frac{(\rho + H_\sigma)^2 + R_{\sigma,G}^2 - (\rho + H_G)^2}{2R_{\sigma,G}(\rho + H_\sigma)} \tag{1}$$

where $\sigma \in \{M, S\}$. Thus, we can have

$$\begin{cases} \sin \theta_{M,G} = \sqrt{1 - \left(\frac{(\rho+H_M)^2 + R_{M,G}^2 - (\rho+H_G)^2}{2R_{M,G}(\rho+H_M)} \right)^2} \\ \sin \theta_{S,G} = \sqrt{1 - \left(\frac{(\rho+H_S)^2 + R_{S,G}^2 - (\rho+H_G)^2}{2R_{S,G}(\rho+H_S)} \right)^2} . \end{cases} \tag{2}$$

Combining (2) with the first three expressions of equation (8) in [1], we obtain

$$\begin{cases} \delta_{M,S} = \arcsin \frac{B \sin \alpha}{\rho + H_S} \\ \delta_{M,G} = \arcsin \frac{R_{M,G} \sin \theta_{M,G}}{\rho + H_G} \\ \quad = \arcsin \left(\frac{R_{M,G}}{\rho+H_G} \sqrt{1 - \left(\frac{(\rho+H_M)^2 + R_{M,G}^2 - (\rho+H_G)^2}{2R_{M,G}(\rho+H_M)} \right)^2} \right) \\ \delta_{M,G} - \delta_{M,S} = \arcsin \frac{R_{S,G} \sin \theta_{S,G}}{\rho + H_G} \\ \quad = \arcsin \left(\frac{R_{S,G}}{\rho+H_G} \sqrt{1 - \left(\frac{(\rho+H_S)^2 + R_{S,G}^2 - (\rho+H_G)^2}{2R_{S,G}(\rho+H_S)} \right)^2} \right) . \end{cases} \tag{3}$$

Therefore, equation (9) in [1] is also incorrect, and the correct expression should be

$$\arcsin \left(\frac{R_{M,G}}{\rho+H_G} \sqrt{1 - \left(\frac{(\rho+H_M)^2 + R_{M,G}^2 - (\rho+H_G)^2}{2R_{M,G}(\rho+H_M)} \right)^2} \right)$$

$$- \arcsin \left(\frac{R_{S,G}}{\rho+H_G} \sqrt{1 - \left(\frac{(\rho+H_S)^2 + R_{S,G}^2 - (\rho+H_G)^2}{2R_{S,G}(\rho+H_S)} \right)^2} \right)$$

$$= \arcsin \frac{B \sin \alpha}{\rho + H_S} . \tag{4}$$

These errors appear not only in [1] but also in equations (8) and (9) of [2] by the same authors. The authors of [1] and [2] have confirmed that the mentioned errors are merely a consequence of a typo and that they did not propagate into the computations and thus did not affect the results [3].

REFERENCES

[1] D. O. Nitti, R. F. Hanssen, A. Refice, F. Bovenga, and R. Nutricato, "Impact of DEM-assisted coregistration on high-resolution SAR interferometry," *IEEE Trans. Geosci. Remote Sens.*, vol. 49, no. 3, pp. 1127–1143, Mar. 2011.

[2] D. O. Nitti, R. F. Hanssen, A. Refice, F. Bovenga, G. Milillo, and R. Nutricato, "Evaluation of DEM-assisted SAR coregistration," in *Proc. SPIE*, Sep. 2008, vol. 7109, pp. 710919-1–710919-14.

[3] D. O. Nitti, R. F. Hanssen, A. Refice, F. Bovenga, G. Milillo, and R. Nutricato, Private communication, Jun. 2011.